Title
RFID-Inspired Miniature Antennas for Circular Polarization Tags and Brain-Machine Interface Applications

Author
Song, Lingnan

Publication Date
2016

Peer reviewed|Thesis/dissertation

University of California
Los Angeles

RFID-Inspired Miniature Antennas for Circular Polarization Tags and Brain-Machine Interface Applications

A thesis submitted in partial satisfaction
of the requirements for the degree
Master of Science in Electrical Engineering

by

Lingnan Song

2016

Abstract of the Thesis

RFID-Inspired Miniature Antennas for Circular Polarization Tags and Brain-Machine Interface Applications

by

Lingnan Song

Master of Science in Electrical Engineering

University of California, Los Angeles, 2016

Professor Yahya Rahmat-Samii, Chair

Radio frequency identification (RFID) technology in the ultra-high frequency (UHF) band has become the mainstream applications that help the speed of handling manufactured goods and materials in recent years. The mechanism of RFID backscattering technique has also been utilized for many novel wireless sensing applications, such as remote health sensing, and biomedical signal recoding. In an RFID system, the tag antenna plays a key role in the overall system performance. In this sense, the study of novel tag antenna design with compact size and circular polarization (CP) characteristics is necessary to achieve miniature and highly-sensitive RFID systems. In the first part of the thesis, we present a CP cross-dipole RFID tag antenna with miniature design. The CP mode is excited by two orthogonal dipoles with 90 degree phase delay between each other. Impedance matching is achieved using a matching structure of T-match meander line. In the second part of the thesis, we present an optimized implantable antenna transferring power and data efficiently with a low profile external transmitting antenna by utilizing RFID backscattering technique. We characterize the coupling enhancement by simulating the wireless link with head models. Prototypes are measured and characterized in terms of absorption level and channel capacity. The proposed antenna system provides wireless and fully-passive solution for multichannel neural recording systems.

The thesis of Lingnan Song is approved.

Tatsuo Itoh

Yuanxun Ethen Wang

Yahya Rahmat-Samii, Committee Chair

University of California, Los Angeles

2016

To my beloved family.

Table of Contents

List of Figures

List of Tables

Acknowledgments

First I would like to express sincere gratitude to my advisor Professor Yahya Rahmat-Samii for his guidance for my Master's study. With his passion and wisdom, he shows me what is needed to be a researcher.

I would like to acknowledge Professor Leena Ukkonen at Tampere University in Finland, for her kindly support, valuable feedback and inspiration on my research.

I would also like to thank my friends and colleagues at UCLA Antenna Research, Analysis, and Measurement Laboratory. It's been my great pleasure working with them.

Finally, I would like to thank my family and my boyfriend, for their love and unconditional support that get me through each challenge. I love them from the bottom of my heart.

CHAPTER 1

Introduction

1.1 Research Background

Communication by means of backscattering power was first demonstrated in 1948 by Harry Stockman [1]. In 1950 the first patent was lodged for passive transponders. For the first time, it had commercial usage in animal tracking in the United States, followed by RFID tracking of US rail cars in 1994. After the establishment of the first Auto ID research center at the Massachusetts Institute of Technology in 1999, research in RFID technology received a huge boost up. Absence of other related technologies like database management and also the absence of any global standards restricted the development of this technology in the initial phase. This problem was solved when EPC Global systems was established in 2003, which was the biggest boost up that this technology received, followed by the market demands of Wal-Mart, US Department of Defense, Gillette, and so on [2].

An RFID system is composed of two core components: an RFID reader, and an RFID tag, which is consist of RFID chip and RFID tag antenna. The tag antenna plays a key role in the overall system performance in terms of read range and overall size, since passive tags are essentially obtaining energy from the incoming radio frequency signal received by the tag antenna. To date, many miniaturized tag antennas have been proposed to achieve compact and sensitive design for RFID transponders [5–9]. Yet most of them are linearly-polarized (LP) antennas, which would result in the 3 dB sensitivity degradation due to polarization mismatch between tag and reader antenna since most of the commercial reader antennas have circular-polarization (CP) characteristics.

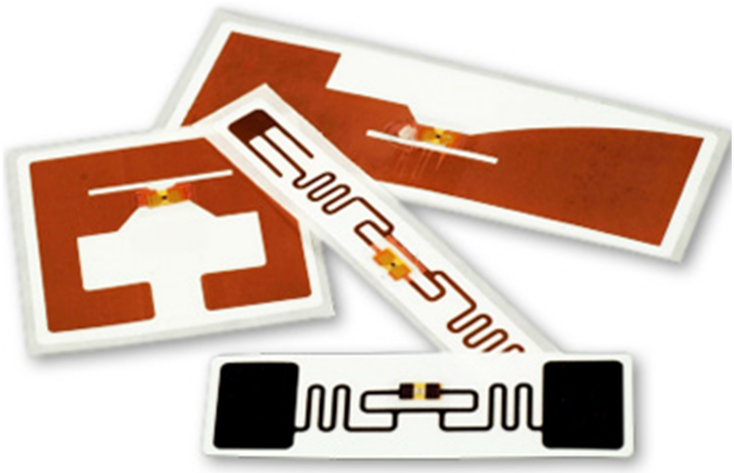

Figure 1.1: RFID products in the market [3, 4].

To address the 3 dB polarization mismatch, various types of tag antennas with CP radiation have been considered. However, most of them are limited by their large size or the need for a high-dielectric substrate, which would make the transponder bulky and limited for real applications [10–13]. In this sense, the study of novel tag antenna design with compact size and CP characteristics is necessary to achieve miniature and highly-sensitive RFID systems.

On the other hand, the mechanism of RFID backscattering technique has been utilized for many novel wireless sensing applications, such as advanced vehicle monitoring, remote health sensing, and biomedical signal recoding [14–16]. Since all the power required for transmission of the sensing data by the transponder is drawn from the electromagnetic power radiating by the reader, it is particularly attractive for sensing systems requiring fully passive operation and comparative small device.

One of these applications involves the emerging field of Brain-machine interfaces (BMIs), which aims at giving severely paralyzed people another way to communicate with the world [18]. This is achieved with devices that record and decode neural signals and control artificial actuators [19]. Currently, one of the major challenges is to develop viable neural interfaces that can work stably and last for a lifetime. The neural implant electronics should thus be wirelessly powered, with ultra-low power consumption, and support reliable data flow to

Figure 1.2: The utilization of RFID technology benifits the development of modern healthcare devices [17].

"read" from the brain.

Considering the system requirements of wireless and fully-passive operation and ultra-low power consumption, the RFID inspired backscattering technology is one of the most promising and safest methods for establishing wireless power and data link to communicating with miniature neural implants [20,21]. Similar to any passive RFID tags, the neural recoding IC obtains power from the carrier signal transmitted by the reader, and the recorded data can be superimposed on carrier signal by modulating terminal impedance of the implanted antenna and backscattered to the reader. In such system, the complexity and power consumption is predominantly at the interrogator, which enables the implementation of battery-free neural implants resembling RFID tags.

1.2 Research Outlines and Goals

1.2.1 Cross-Dipole RFID Tag Antennas

In the first part of the thesis, a circularly polarized cross-dipole antenna for UHF RFID tag is presented. The antenna structure was inspired by [22].The antenna is miniaturized with dimensions of 35.6 × 35.6 × 0.78 mm^3 The CP mode is excited by two orthogonal dipole branches with 90 degree phase delay between each other. Impedance matching between tag antenna and the chip is achieved using a matching structure of T-match meander line [23]. The triangular-shaped ending is used for achieving a compact size [24, 25]. The structure was simulated and optimized using particle swarm optimization (PSO). The design goal is to achieve good sensitivity with compact design. The following criteria is assigned:

1) To achieve satisfactory impedance matching of S_{11} less than -10 dB between tag antenna and tag chip to minimize return loss.

2) To miniaturize the antenna area to less than 20 cm^2, length smaller than 7 cm and substrate thickness less than 5 mm.

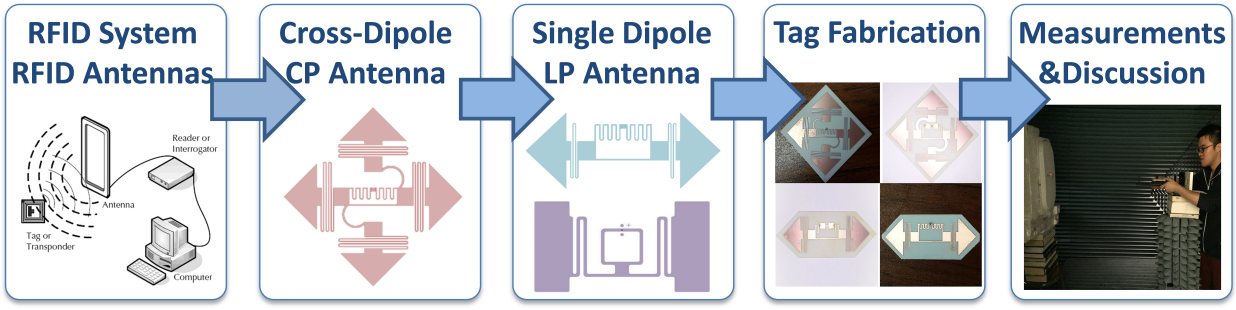

Figure 1.3: Flow chart for the study of CP cross-dipole RFID tag antennas.

The first part of the thesis starts with a brief introduction about RFID systems in Chapter 2. RFID backscattering mechanism is then introduced and RFID tag antenna design criteria is specified. In Chapter 3, design and measurements of the cross-dipole RFID tag antenna is presented, followed by discussion based on measurement results.

1.2.2 BMI Antennas based on RFID-Inspired Backscattering Technique

In the second part of the thesis, an antenna system for wireless neural recording based on RFID inspired backscattering technique was proposed. Power and data transfer is achieved by near field inductive coupling between transmitting antenna and implanted antenna. The power received by the implanted antenna will activate the neural recording IC. Just like the operating mechanism of any passive RFID tags, the data link is established through the modulation of the impedance at the terminal the implant antenna according to the acquired neuro signal. This study was inspired by the research work reported in [20].

In this study, we design and characterize a miniature implantable antenna that is optimized to communicate with an external transmitting antenna at the Medical Implant Communications Service (MICS) frequency band (402-405 MHz), which is a part of the spectrum that has the characteristics favorable to the transmission of radio signals into the human body [26].

The wireless inductive link between transmitting and implanted loop antennas with head tissue in between was modeled as a linear two-port network [27]. The coupling efficiency between antennas is described by the link power gain $G_{p,max}$, which is the ratio of the power delivered to the implanted microsystem to the power supplied to the external transmitting antenna as the two ports are simultaneously conjugate matched [28].

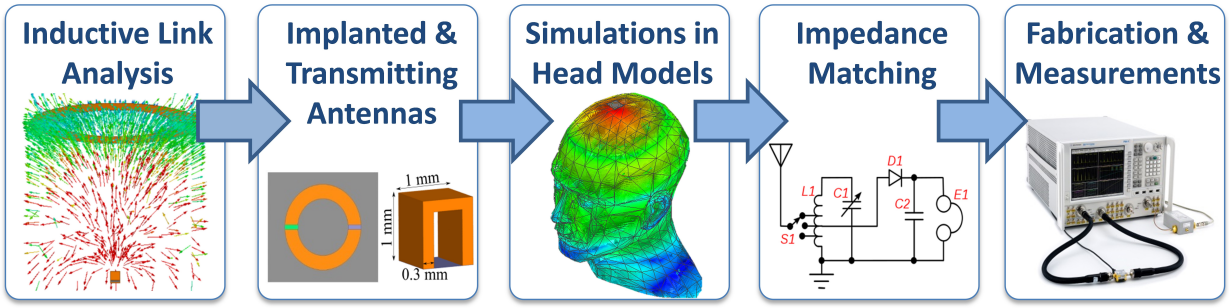

Figure 1.4: Flow chart for the study of BMI antennas based on RFID-inspired backscattering technique.

Theoretical analysis of the wireless inductive link between a low-profile interrogator loop

antenna and the implanted antenna is presented first in Chapter 4, followed by discussion focusing on antenna design of transmitting and implanted loop antennas to achieve high magnetic coupling and low SAR. Simulation results of the coupling link power efficiency between transmitting and implanted antennas presented in different human head model are shown in Chapter 5. Finally performance of the antennas was validated by measurements and results are presented in Chapter 6 and further evaluated regarding the specific absorption rate (SAR) generated in tissue and channel capacity from both power and data point of view, proving the feasibility of this approach.

CHAPTER 2

RFID Systems and RFID Tag Antennas

2.1 Introduction to RFID Systems

Radio-Frequency Identification (RFID) is a wireless data capturing technique from a tagged item. An RFID system consists of an interrogator (reader) and a tag or transponder [2]. RFID tags or radio transponders are high-frequency electronic devices that broadcast the position or attributes of specific items to which they are attached, which allows these items of interest to be remotely detected, identified, and tracked. In a broader perspective, RFID technique falls into the specialized category of Automatic Identification (Auto ID) that uses an electromagnetic signal to communicate between the reader and the transponder [29].

Auto ID technology is a big superset of different technologies including Magnetic Ink Character Recognition (MICR), Voice Recognition, Biometrics, Barcodes, and RFID. Among the various forms of Auto ID, optical barcodes have been dominating the Auto ID market and are widely used in almost everything and everywhere, which is mainly because of their low cost. However, barcodes are limited in memory storage capabilities; and based on the line-of-sight operating mechanism, barcode has to be presented in the "sight" of reader, which means the reading distance is limited.

RFID technology comes into the Auto ID market with huge potential of overcoming these limitations. However, RFID tags require a silicon chip to store the data, which makes the tags expensive comparing with barcodes. Hence the momentum arises for the need of RFID tags with large reading distance, large data storage capability and low cost.

The basic RFID system consists of three components: (i) a miniature tag device (or transponder) attached to the item of interest, (ii) a reader (or transceiver) whose location

is generally fixed and which contains an attached antenna. The system operates as follows: signal with unmodulated periods is transmitted by the reader through its attached reader antenna. The tag receives the signal, extracts DC power from the unmodulated period to power the IC, and responds the reader either by reading or writing data, which typically would be an identity code or a measurement value. The tag may also resend the original signal received from the reader, with a predetermined time delay.

The unique identification of the object to be tracked is stored in IC. The major difference among the different Auto ID technologies is in how identification is stored and retrieved and how less frequent is the human intervention. This is where RFID technology has advantages over all other existing Auto ID technologies in terms of ease and areas of application and subsequently became a major topic of research in these current years.

2.2 RFID Transponder Design Specifications

In an RFID system, the reader or interrogator is usually fixed and only need to be installed one time, whereas the tags or transponders are required in thousands or millions, depending on the application. Thus research on tags with desirable and stable performance is essential for the wide-spread usage of RFID technology. When designing an RFID tag or transponder, the following characteristics need to be considered carefully [2].

2.2.1 Frequency of Operation

RFID is typically considered as a non-specific short range device. It can use frequency bands without a license. Nevertheless, design of RFID tags has to be compliant with local regulations [30].

- Low frequency (LF): 125-134 kHz

  RFID LF tags are well adapted for animal tracking, patients tracking, veichle immobilizer, and so on. Glass tags are small and light. They can be used with all kinds of material - textiles, metals, plastics etc. Generally these tags are passive tags with

short read range (a few inches).

- High frequency (HF): 13.56 MHz

  RFID HF tags are used in traceability and logistics applications, using loop antenna printed or etched on flexible substrates. They are passive tags with longer read range of about 3 ft.

- Ultra-high frequency (UHF): 860-960 MHz

  Globally, each country has its own frequency allocation for passive UHF RFID, e.g. 866-869 MHz in Europe, 902-928 MHz in North and South America, 950-956 MHz in Japan and some Asian countries [31].

  RFID UHF tags typically have dipole like antennas etched or printed on all kind of dielectric substrate, using backscatter coupling to communicate with reader. The read range of such a tag can be comparably far, around 3 to 6 or even 8 meters. Specific antenna design is required for metallic environments.

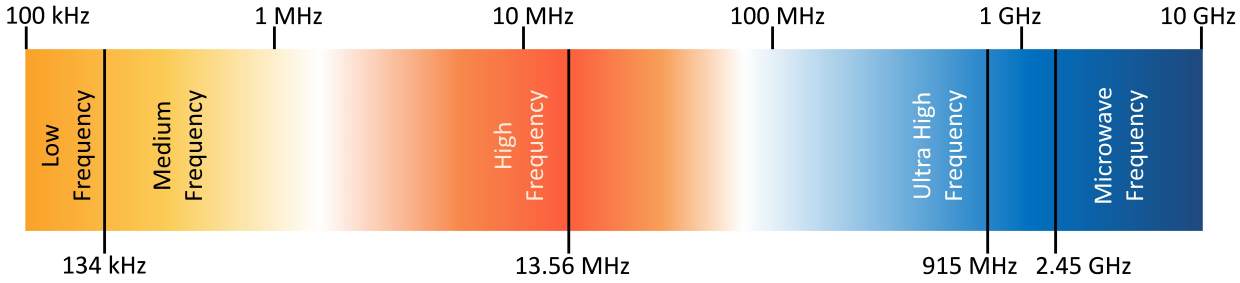

Figure 2.1: RFID frequency spectrum table.

2.2.2 Near-Field vs Far-Field Coupling

In an RFID system, communication between interrogator and transponder is achieved by transferring electromagnetic (EM) energy through coupling, which can be categorized into two types, by the region of field where the coupling occurs [2].

- Near-Field/ Inductive Coupling:

  Near-field coupling occurs where the plane wave has not yet fully developed and separated from the antenna. The distribution of the near field is fairly omnidirectional, and the power attenuates at the sixth power of the distance from the antenna. This is basically a transfer of energy through shared magnetic field and hence operation is limited to only LF and HF frequencies and only RFID tags. The wavelength is much bigger than the antenna and the interrogation zone. The antennas operating in the near-field region are always inductive coil.

- Far-Field/ Backscattering Coupling:

  Far-field coupling occurs in area beyond near field region and communication between tag and reader is achieved by backscattered EM radiation. In the far field, EM power attenuates in a radial manner obeying the inverse square law of distance from the antenna.The EM energy is transmitted from the reader antenna and received by the tag antenna, where it is reflected back with information of tag modulated into the signal. The signal is then detected, amplified, and decoded to extract the data. This kind of communication is prevalent in the UHF passive RFID tags.

2.2.3 Read Range and Link Budget

The most important tag performance criteria is read range. In an RFID system, read range is defined by the distance between reader and tag from which the tag can be detected and read. Read range depends on multiple factors, including the frequency of operation, the size of tag antenna, the power level of reader and whether the tag is active or passive. Link budget calculation in wireless communications specifies the required power budgeting for the transmitter and receiver, the antenna gain, and effective isotropic radiated power (EIRP) of the reader antenna to obtain a certain level of read range. It helps RFID antenna designer to evaluate the required antenna specifications to obtain robust communication in the specific wireless application.

2.3 RFID Backscattering Mechanism

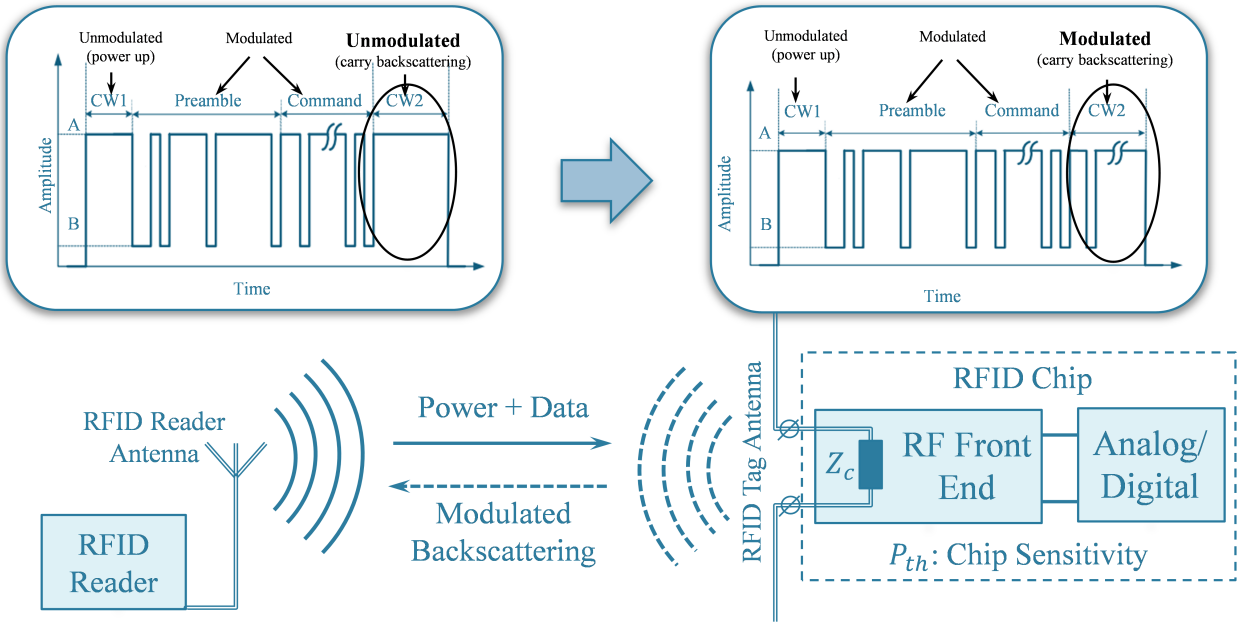

Figure 2.2: Operating mechanism of a basic RFID system.

In this section, we focus on theoretical analysis of far-field backscattering mechanism in passive RFID systems. As illustrated in Fig. 2.2, a passive backscattering RFID system operates as follows [31]:

- First the RFID reader transmits a modulated signal with periods of unmodulated carrier to power up the passive tag.
- The RF voltage developed on antenna terminals during the unmodulated period is converted to DC and powers up the chip.
- The RFID chip sends back the information by varying its front end complex input impedance, effectively modulating the backscattered signal.

In the figure, Z_c is the port impedance of chip. P_{th} is the chip sensitivity, representing the minimum threshold power necessary to provide enough power to activate the RFID chip. Typically the read sensitivity $P_{th,read}$ is smaller than the write sensitivity $P_{th,write}$.

In a passive RFID system, read range of a tag is affected by the chip sensitivity, impedance matching, and also factors such as tag orientation, material and environment. Read range can be calculated by Friss free-space equation as:

$$r = \frac{\lambda}{4\pi}\sqrt{\frac{P_t G_t G_r \tau \tau_{PLF}}{P_{th}}} \tag{2.1}$$

where r is the read range, λ is the wavelength, P_t is the transmitted power by reader, G_t is the gain of reader antenna, G_r is the gain of tag antenna, τ_{PLF} is the polarization loss factor (see Appendix A), and τ is the transmission coefficient defined by:

$$\tau = \frac{4real(Z_c)real(Z_a)}{|Z_c + Z_a|^2}, 0 \leq \tau \leq 1 \tag{2.2}$$

where Z_a is the port impedance of tag antenna attached to IC. The transmission coefficient refers to the power loss by reflection due to mismatch.

2.4 UHF RFID Tag Antenna Design Specifications

In an RFID system, antennas are the spatial filters since they form certain radiation pattern to couple the free space electromagnetic energy into guided structures to enable communication between reader and tags located at certain directions [29]. In this section, we discuss various aspects of antenna design for UHF RFID tags.

2.4.1 Frequency and Bandwidth

The antenna impedance, chip impedance, and read range are all functions of frequency for a typical RFID tag. The frequency of the peak range is referred as the tag resonance. The tag range bandwidth can be defined as the frequency band in which the tag offers an acceptable minimum read range over that band.

2.4.2 Impedance Matching

Among all the other factors, impedance matching plays a key role in RFID tag antenna design. The design and manufacturing of new application-specific integrated circuits (ASICs)

is both time and cost consuming in industry, thus RFID antennas are typically designed for specific ASICs in market. Since the IC attached to the tag antenna terminals are typically built with capacitive impedance, the design goal of tag antenna is to achieve inductive input reactance required for conjugate matching with IC. The common impedance matching technique is usually not applicable here since incorporating matching network with lumped elements would increase the cost of manufacturing. To overcome this, matching mechanisms have to be adopted to tag antenna layout.

One of the most popular strategy of tuning antenna impedance is the well-known T-matching technique, which tunes the impedance of dipole antenna by introducing a centered short-circuit stub [32]. The T-matching strategy is illustrated by Fig. 2.3.

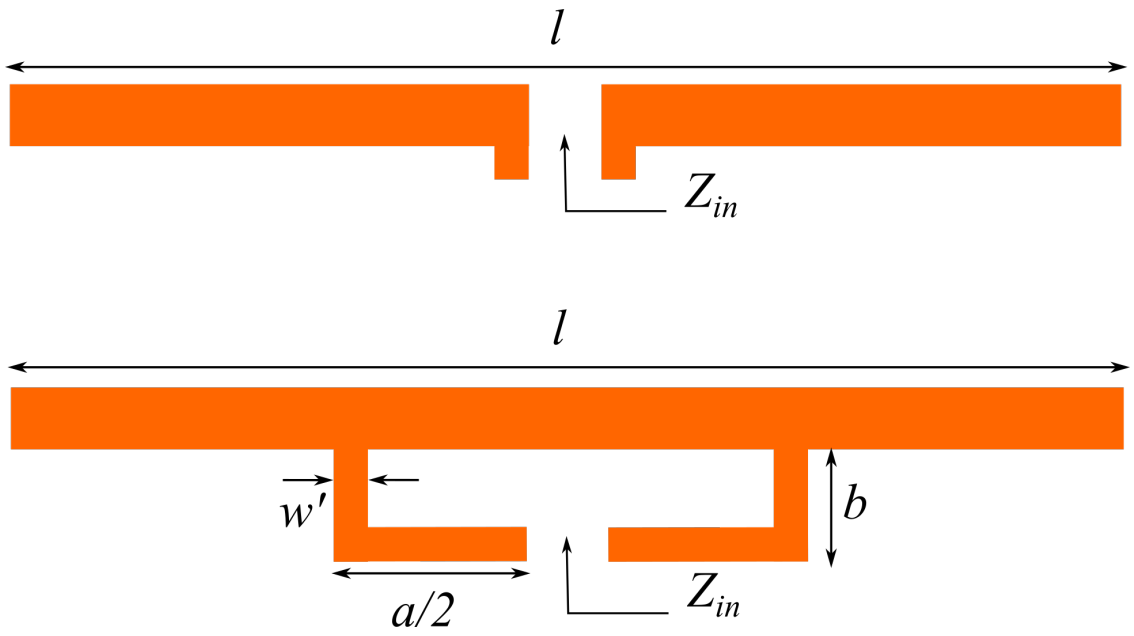

Figure 2.3: T-matching structure for tuning inductive impedance of planer dipole antennas. The geometrical parameters a, b, and w' can be tuned to match the IC impedance.

2.4.3 Polarization

The polarization of any antenna is defined by the polarization of the electrical field it radiates, which may be linear, circular or elliptical. Reader antennas are typically circularly polarized,

while most tag antennas are linearly polarized dipole-type antennas. Comparing with linearly polarized tags, circularly polarized ones have advantages in the sense that tags can be read in any orientation, with a 3-dB enhancement of power level at maximum. Another very big advantage of the circularly polarized antennas is the fact that they can operate in the close proximity without any interference if their senses of polarization are opposite (e.g. one left-handed and the other right-handed). Readers with opposite polarizations placed alternately are very helpful in dense reader environments where lot of readers have to be accommodated to accurately and quickly read any tag that might be passing through. The polarization mismatch between antennas is discussed in Appendix A.

2.4.4 Gain and Directivity

In an RFID system, the reader antenna is usually required to have large gain and directivity, whereas the tag antennas are supposed to achieve omnidirectional operation (except for the cases where the tags are mounted on metallic surfaces). This is important in determining the interrogation zone of an RFID tag.

In conclusion, when one designs an RFID tag antenna, the tradeoffs between antenna size, gain, polarization, impedance, and bandwidth need to be carefully evaluated. Generally the design requirements are largely determined by the specific application as well as characteristics of reader antenna.

CHAPTER 3

Meander Dipole RFID CP Tag Antennas: Design and Measurements

In this chapter, a compact circularly polarized (CP) crossed-dipole antenna for radio frequency identification in the ultra-high frequency is studied. The CP mode is excited by two orthogonal dipoles with 90 degree phase delay between each other. Impedance matching between tag antenna and the chip is achieved using a matching structure of T-match meander line. The triangular-shaped ending is used for achieving a compact size [22]. The structure was simulated and optimized using particle swarm optimization (PSO).

3.1 RFID Chip and Reader Specifications

In this chapter, we study RFID tag antennas designs based on the following commercial RFID tag chip and RFID reader:

3.1.1 Monza 5 RFID Chip

The Monza 5 UHF RFID tag chip is a commercial RFID chip produced by Impinj. It is optimized for serializing items such as apparel, electronics, cosmetics, documents and jewelry. The Monza 5 tag chip fully supports all requirements of the Gen 2 specification as well as many optional commands and features. In addition, the Monza tag chip family provides enhancements of writing and reading sensitivity and reliability, high speed writing and encoding. Specifications of Monza 5 tag chip are listed in Table 3.1. As shown in Fig. 3.1, Monza 5 tag chips have four external pads available to the user: one RF+ pad, two

RF- pads, and a non-connected pad designated NC. RF+ and RF- form a single differential antenna port [33].

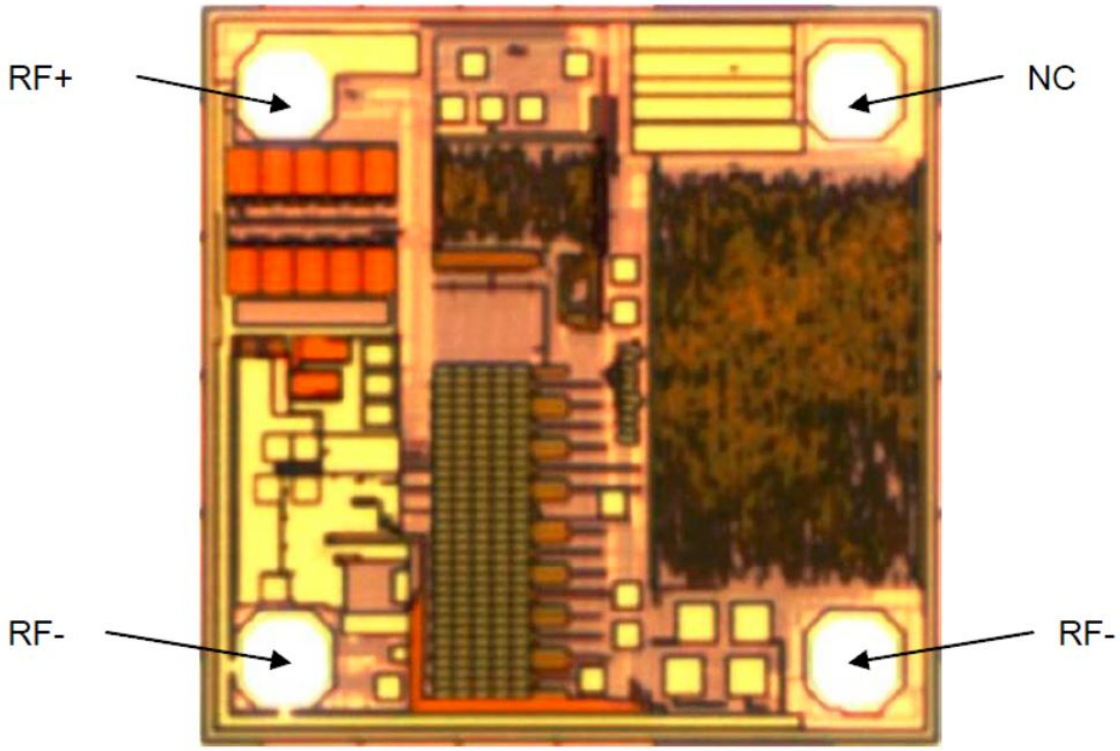

Figure 3.1: Monza 5 tag chip die orientation [33].

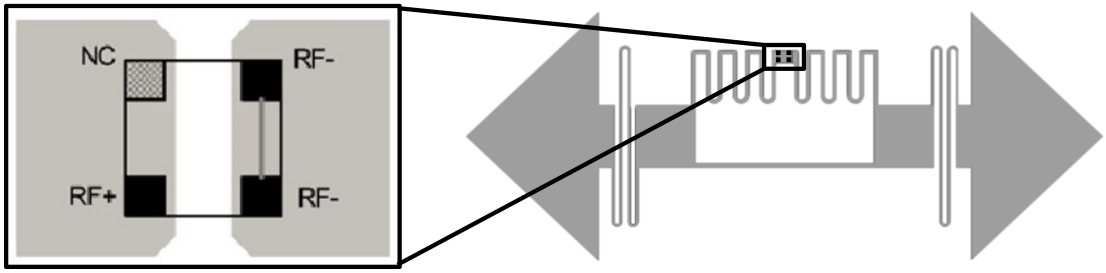

Figure 3.2: RFID chip connected to the antenna differential port.

Table 3.1: Specifications of Monza 5 RFID tag chip [33].

Parameters	Typical Value	Comments
C_p	0.825 pF	Intrinsic chip capacitance
R_p	1.8kΩ	Intrinsic chip resistance
C_{mount}	0.245 pF	Typical capacitance due to adhesive
Z_{chip}	14.562-i 161.24Ω	Total chip impedance
Chip Read Sensitivity	-17.8 dBm	Measured using DSB-ASK modulation
Chip Write Sensitivity	-13.75 dBm	—

3.1.2 NXP G2XM RFID Chip

The NXP G2XM is an RFID chip for passive, intelligent tags and labels supporting the Gen 2 UHF RFID standard. It is suited for applications where operating distances of several meters and high anti-collision rates are required. Specifications are listed in Table 3.2. A unique feature of NXP chip is that it provides package option with Cu or Al straps, which enable the reliable connections between RFID chips and antennas for research purposes (Fig. 3.3) [34].

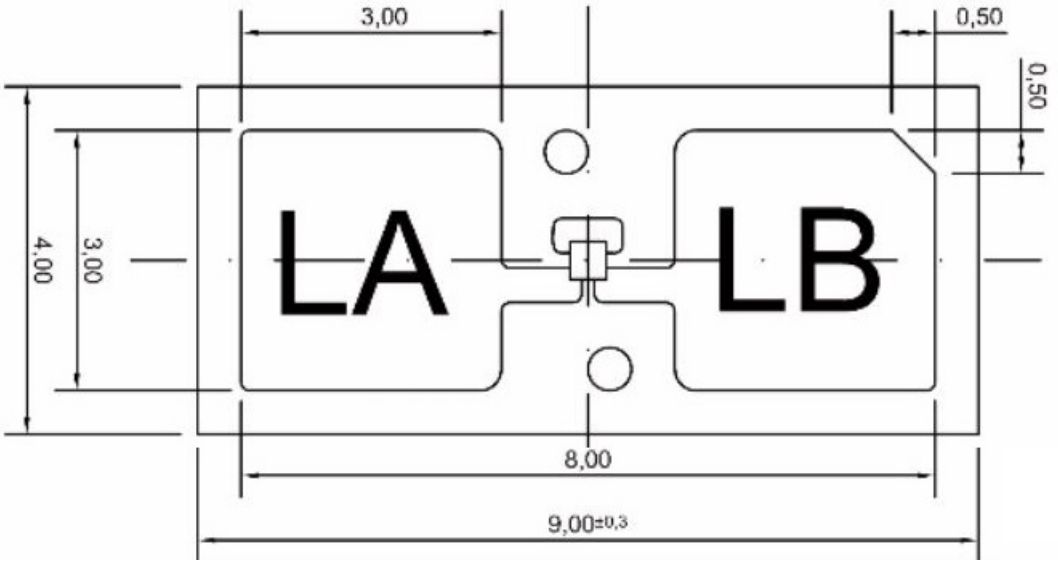

Figure 3.3: NXP chip with straps: layout and pinning [34].

Table 3.2: Specifications of NXP G2XM RFID tag chip [34].

Parameters	Typical Value	Comments
C_i	1.36 pF	Intrinsic chip capacitance with Cu straps
Z_{chip}	14.8-i 128Ω	Total chip impedance with Cu straps
C_i	1.42 pF	Intrinsic chip capacitance with Al straps
Z_{chip}	13.3-i 122Ω	Total chip impedance with Al straps
Chip Read Sensitivity	-15 dBm	minimum operating power supply

3.1.3 Mercury 4 RFID Reader and Antenna

The Mercury 4 is a low profile, high-performance 4-port RFID reader for both indoor and outdoor applications. Specifications of reader, cable and antenna are listed in Table 3.3, 3.4 and 3.5 [35].

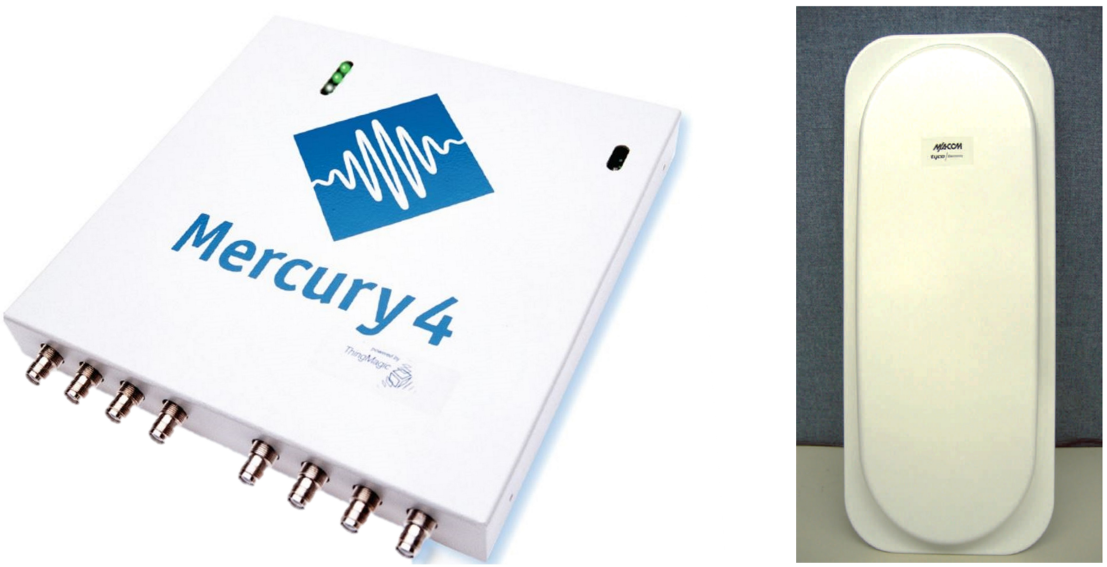

Figure 3.4: Mercury 4 reader and authorized dual-circular-polarized antenna [35].

Table 3.3: Specifications of Mercury4 RFID reader [35].

Frequency	UHF operating frequency: 902-928 MHz
Input voltage	24 Vdc, 2.0 A
Supported UHF Tag Protocols	EPC Class 1, GEN2EPC Class 0

Table 3.4: Specifications of Mercury4 RFID reader cable [35].

Standard	Reverse TNC to Reverse TNC
Length	25 ft.
Insertion Loss	3.1 dB

Table 3.5: Specifications of Mercury4 RFID reader antenna [35].

Model	MANNAT0141
Gain	5.9 dBi max
Connector	Reverse TNC
Polarization	LHCP, RHCP (dual-circularly polarized)

3.2 Circularly Polarized RFID Tag Antenna

In this section a cross-dipole RFID tag antenna design is presented. The design goal is to achieve good sensitivity with compact design. The following criteria is assigned:

1) To achieve satisfactory impedance matching of S11 less than -10 dB between tag antenna and tag chip to minimize return loss.

2) To miniaturize the antenna area to less than 20 cm^2, length smaller than 7 cm and substrate thickness less than 5mm.

The cross-dipole RFID tag antenna was designed to be integrated with the RFID chips specified in previous section. For the requirement of conjugate match the antenna with RFID chip, the input impedance of the proposed antenna must be approximately 14.8 + i 128 Ω (NXP) or 14.562 + i 161.24 Ω (Monza 5). The input impedance of the antenna can be tuned

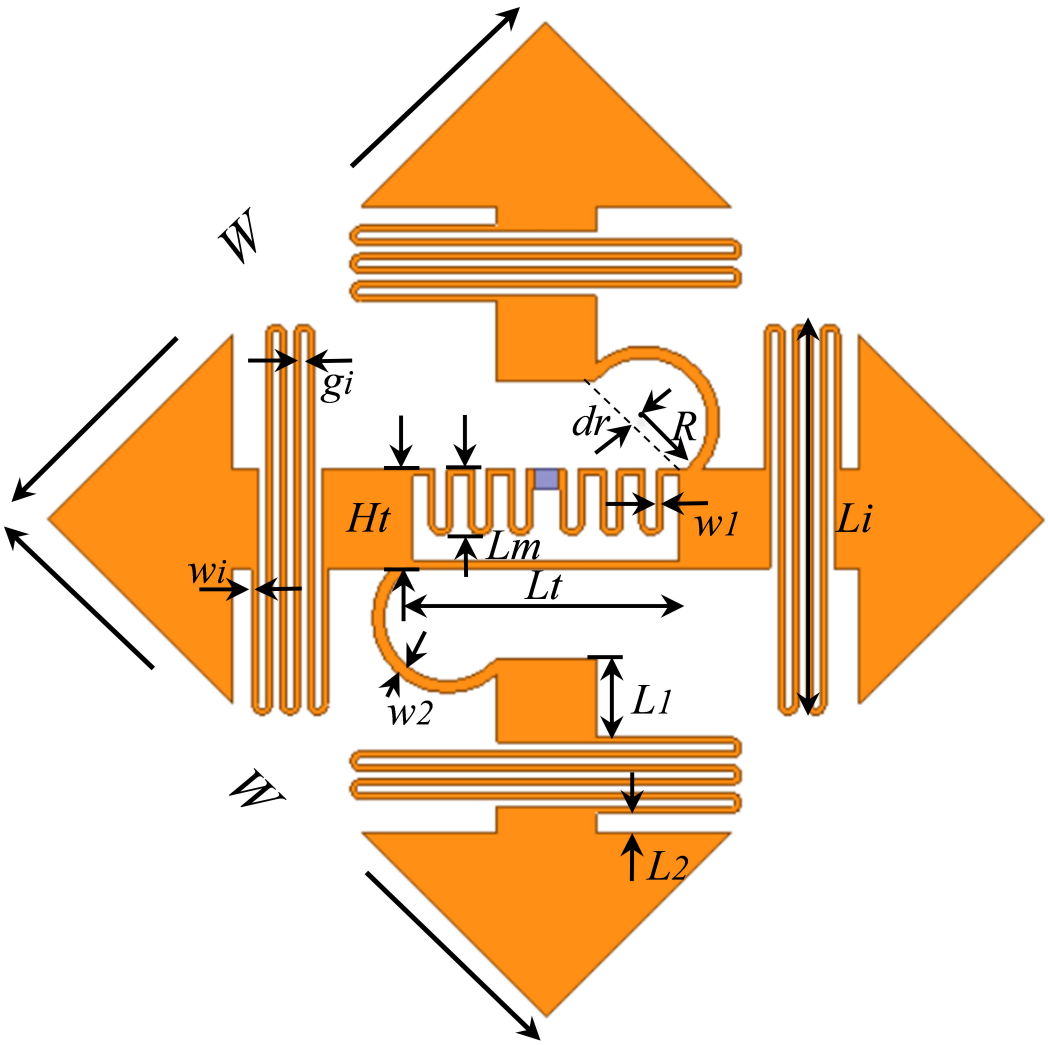

Figure 3.5: Geometry of the meandered cross-dipole RFID tag antenna.

by optimizing the dimensions in the T-match section.

Circularly polarized (CP) radiation of the antenna is achieved by the inserting two semi-circular curves between the orthogonally arranged dipole arms. The two crossed dipoles with orthogonal radiation mode (one horizontal and the other vertical) were tuned to have overlapping resonances that exhibit a 90 phase difference at the frequency of 915 MHz.

The dimensions w1, Lm and Ht were tuned to conjugate match the antenna to different chip impedance. And the dimensions w2 and dr were tuned to adjust the semi-circular rings

to achieve CP radiation. The optimized dimensions for two chips are listed in Table 3.6.

Table 3.6: Geometry of meandered cross-dipole RFID tag antenna.

Parameter	Dimension (NXP)	Dimension (Monza5)	Comments
W	35.6 mm	35.6 mm	fixed
L1	4 mm	4 mm	fixed
L2	1 mm	1 mm	fixed
Li	19.7 mm	19.7 mm	fixed
wi	0.2 mm	0.2 mm	fixed
gi	0.4 mm	0.4 mm	fixed
R	3.2 mm	3.2 mm	fixed
Lt	14 mm	14 mm	fixed
w1	0.4 mm	0.3 mm	optimized
w2	1.6 mm	0.6 mm	optimized
Lm	4.2 mm	3.3 mm	optimized
Ht	8mm	5 mm	optimized
dr	0 mm	0.2 mm	optimized

Fig. 3.6 shows the simulated current distribution of the antenna at 915 MHz for the two phase angles 0° and 90°. We observed that at phase of 0°, the currents are mainly flowing on the vertical branch of the cross-dipole while at phase of 90° the currents are mainly distributed on the horizontal branch. This current arrangement over phase explains the CP radiation of the cross-dipole antenna. Note that the currents distributed on the T-matching section are different for the two phases due the asymmetric antenna structure. The current distribution on the meander line of T-matching section ia larger at phase 0° than at phase 90°.

Fig. 3.7 shows the simulated input impedances of the antenna. Good conjugate matching between the input impedances of the antenna and the RFID chip was observed. The

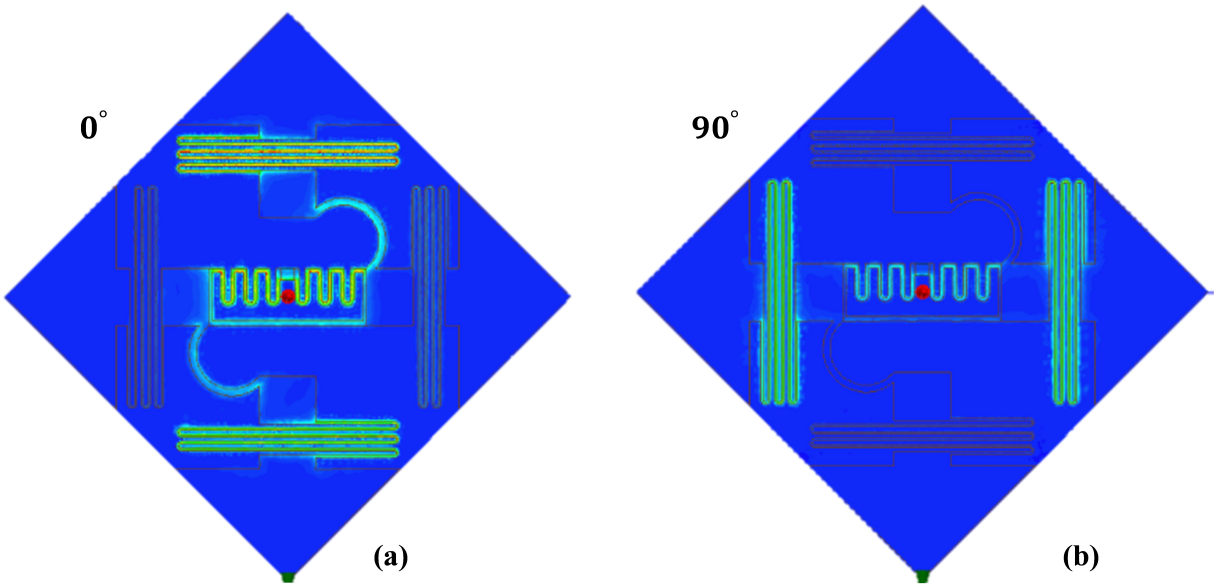

Figure 3.6: Simulated current distribution of the tag antenna at 915 MHz for two phases (a) 0° and (b) 90°

resistance and reactance components of the antenna were very close to those of the chip at around 900-930 MHz. Fig. 3.8 confirmed the good impedance matching bandwidth with the simulated reflection coefficient. For the case of conjugate match, the S_{11} was calculated by:

$$S_{11} = \frac{Z_a - Z_c^*}{Z_a + Z_c} \tag{3.1}$$

where Z_a is the complex impedance of antenna and Z_c is the complex impedance of the chip (see the MATLAB code in Appendix B).

Fig. 3.8 also shows the simulated axial ratio (AR) of the cross-dipole antenna, which is defined as the ratio of the major axis to the minor axis of the polarization ellipse. Simulated results of AR in the direction of $\theta = 0°$ showed that its 3-dB AR bandwidth was 8 MHz (908-916 MHz).

Fig. 3.9 shows the simulated radiation pattern of the antenna at 915 MHz in xz plane. The antenna radiates a left-handed CP (LHCP) on the front side ($\theta = 0°$), and a right-handed CP (RHCP) on the back side (θ=180°). The maximum gain of -3.5 dB was achieved on both sides.

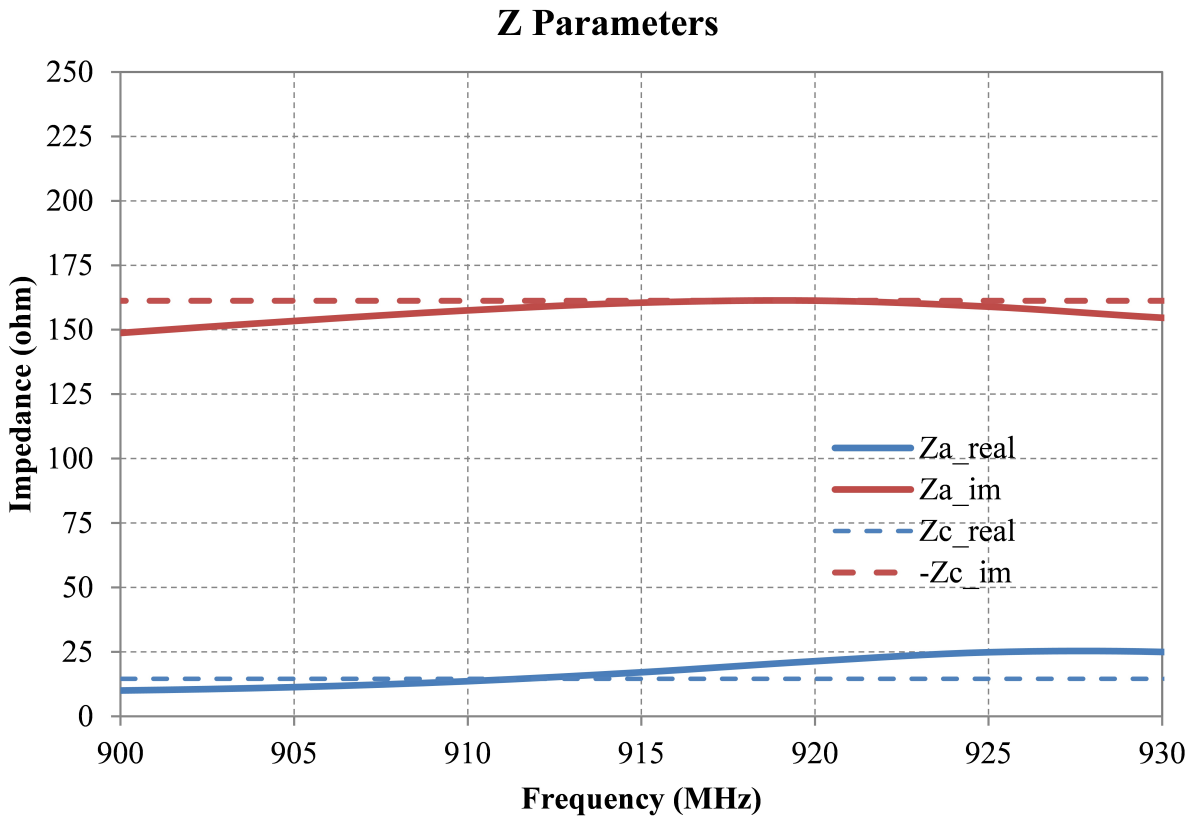

Figure 3.7: Simulated antenna impedance and comparison with the chip impedance (Monza 5).

3.3 Linearly-Polarized RFID Tag Antenna

A linearly polarized (LP) tag antenna was also built to verify the CP performance of the cross-dipole antenna. The LP tag was built by removing a vertical branch and the semi-circular rings. Its impedance and directivity characteristics are similar as the CP counterparts. Dimensions of Ht, Lm, w1 and Li were adjusted to achieve good conjugate matching with the chip. The optimized dimensions are listed in Table 3.7. And simulated S_{11} are shown in Fig. 3.11.

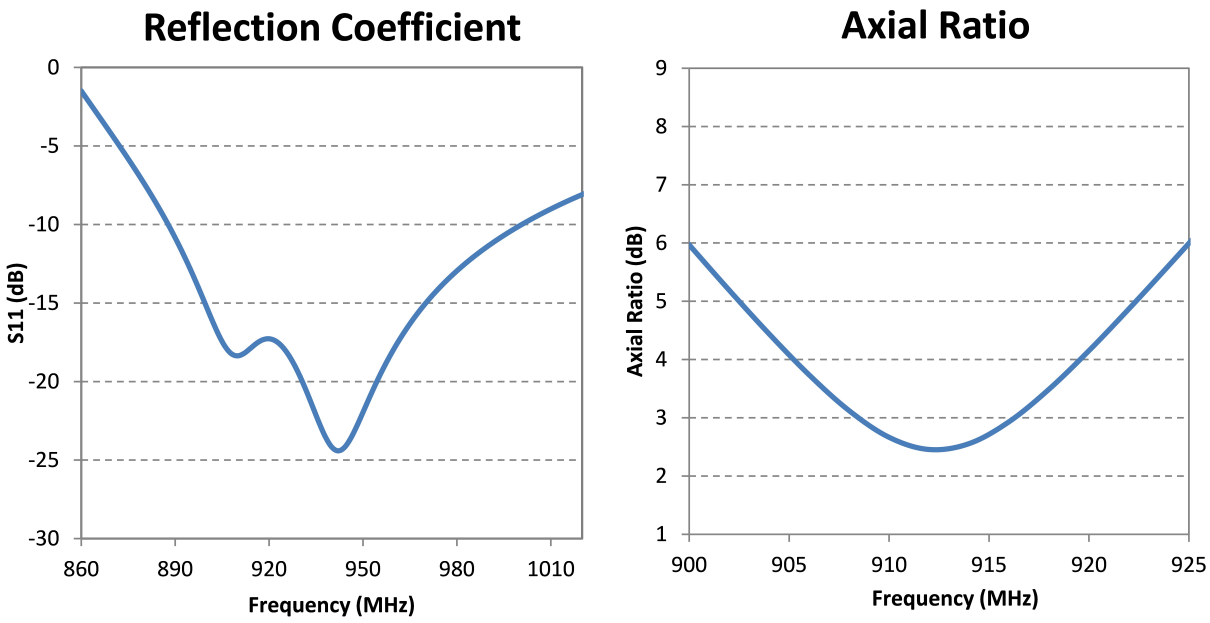

Figure 3.8: Simulated S_{11} and AR ($\theta = 0°$) of the cross-dipole antenna.

Table 3.7: Geometry of LP meandered dipole RFID tag antenna.

Parameter	Dimension (Monza 5)	Comments
Li	14.4 mm	optimized
w1	0.3 mm	optimized
Lm	4.2 mm	optimized
Ht	9.3 mm	optimized

3.4 Particle Swarm Optimization on RFID Tag Antennas

The optimization of RFID tag antennas includes determining input design optimization parameters in RFID tag antenna structures, describing of output antenna performance and design objectives including S_{11} and AR, drawing structure models in EM simulators, simulating by full-wave EM solvers, and adjusting of the input parameters according to the output simulation results. Nature-inspired global optimization, specifically particle swarm optimization (PSO) was employed [36] to optimize the tag antenna geometries.

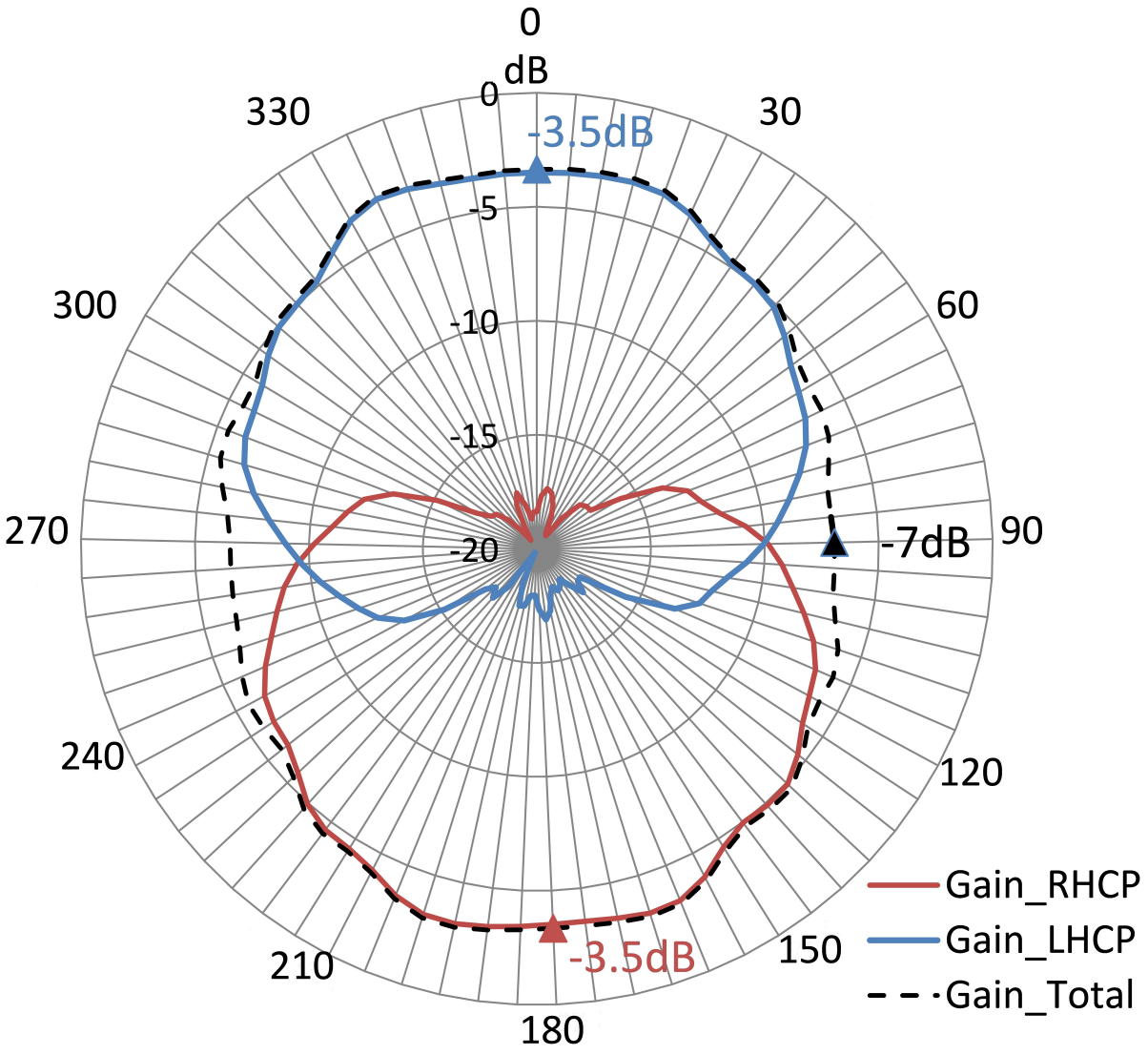

Figure 3.9: Simulated radiation pattern of the cross-dipole antenna.

Both CP and LP tag antennas presented in 3.2 and 3.3 were optimized with dimensions specified in Table 3.6 and 3.7. The fitness function for the CP antenna is given by:

$$Fitness_{CP} = 50 - 10(1 - |S_{11}|^2_{f=915MHz}) \cdot \frac{1}{1 + e^2|_{f=915MHz}} \tag{3.2}$$

where e is defined by the axial ratio (AR) in Appendix A as:

$$e = \frac{AR - 1}{AR + 1} \tag{3.3}$$

AR and S_{11} are the axial ratio and reflection coefficient in real values simulated at 915

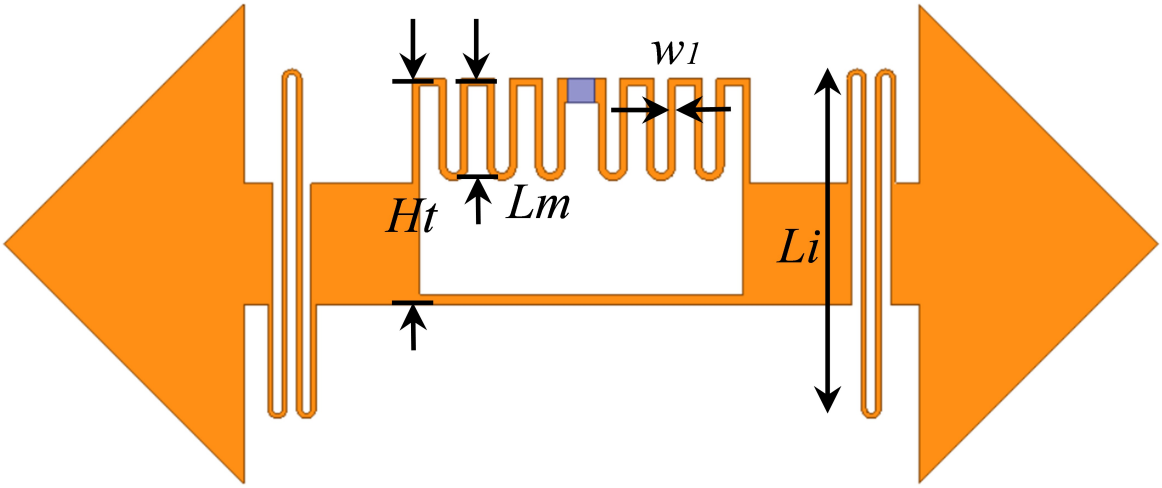

Figure 3.10: Geometry of the LP RFID tag antenna.

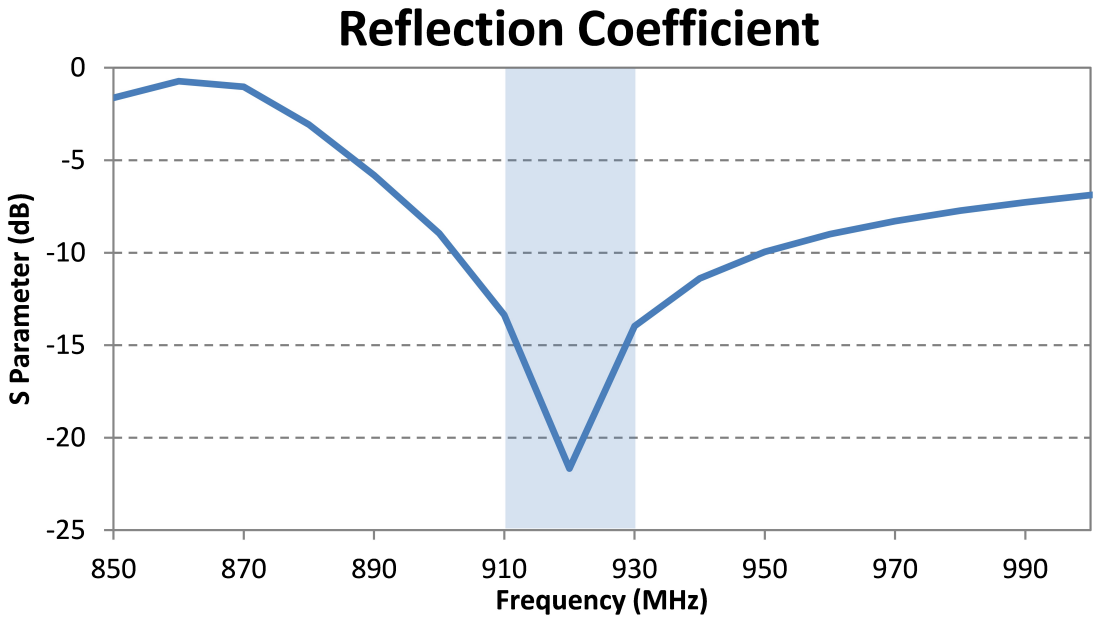

Figure 3.11: Simulated S_{11} of the LP RFID tag antenna.

MHz. The desired AR value is close to 1.4 (3 dB) and the desired S_{11} is close to 0.312 (10 dB). The fitness function for the LP antenna is given by:

$$Fitness_{LP} = 50 - 10(1 - |S_{11}|^2_{f=915MHz}) \cdot Gain|_{\theta=0,f=915MHz} \tag{3.4}$$

where S_{11} and $Gain$ are the reflection coefficient and broadside gain in real values simulated at 915 MHz.

3.5 Measurement Setup

3.5.1 Read Range Measurement

The read range measurement is an application-specific measurement for RFID tags. Besides the antenna itself, the measured read range is also related to the features of RFID reader, reader antenna, and the transmitting power level. Read range is defined as the maximum activation distance of the tag along a specific direction as [37]:

$$d_{max}(\theta, \phi) = \frac{c}{4\pi f}\sqrt{\frac{EIRP}{P_{chip}}G_{tag}(\theta, \phi)} \tag{3.5}$$

where EIRP is the effective isotropic radiated power transmitted by the reader and P_{chip} is the read or write sensitivity of the RFID chip. For read range measurement, it requires that an RFID chip be physically connected at the tag antenna's balanced terminals. Measurements should be performed in a controlled environment such as an anechoic camber, as shown in Fig. 3.12.

In the read range measurement, instead of using the equation above, another expression can also be used to find the maximum read range for a certain EIRP:

$$d_{max} = d\sqrt{\frac{EIRP}{P_{min}G_tL_c}} \tag{3.6}$$

where d is a fixed distance in measurement and P_{min} is the minimum transmitting power required to activate the tag at distance of d. G_t is the reader transmitting antenna gain and L_c is the insertion loss of reader antenna cable.

The read range measurement is the simplest to perform. It only requires an RFID reader with tunable power level and desired polarization characteristics. The read range

measurement provides a true system performance evaluation. However, the features of the tag antenna, such as impedance, directivity and polarization, are hidden within the overall results [32].

3.5.2 Differential Port Impedance Measurement

The majority of the RFID tag antennas are balanced designs. The impedance of a balanced antenna can hardly be measured directly by a typical VNA which is terminated with unbalanced coaxial ports. If the balanced RFID was directly connected to the unbalanced coaxial port, then the currents fed into the two sections of the antenna are unequal, which would make the measured antenna impedance inaccurate. A straightforward way to address the problem is to connect the balanced antenna to unbalanced ports through a balun, which creates equal currents flowing into the two sections. However, careful attention needs to be paid as the unideal balun is introduced into the measurement setup.

In this study we used a method based on two-port S parameter measurement to characterize the balanced RFID antenna impedance. This method is able to characterize asymmetrical balanced antenna impedance precisely without introducing baluns. Together with the coaxial fixture and the port-extension technique, the impedance of the antennas can be extracted directly from the measured S-parameters over broad frequency band [38].

Referred to Fig. 3.13, the impedance of the balanced antenna can be expressed as follows [39]:

$$Z_d = \frac{V_d}{I_0} = \frac{V_1 - V_2}{I_0} = \frac{(Z_{11}I_1 + Z_{12}I_2) - (Z_{21}I_1 + Z_{22}I_2)}{I_0} \tag{3.7}$$

Since $I_1 = I_0$ and $I_2 = -I_0$, the results in (3.7) can be simplified as:

$$Z_d = Z_{11} - Z_{21} - Z_{12} + Z_{22} \tag{3.8}$$

Converting the Z-parameters to S-parameters, the balanced antenna impedance can be expressed as:

$$Z_d = \frac{2Z_0(1 - S_{11}S_{22} + S_{12}S_{21} - S_{12} - S_{21})}{(1 - S_{11})(1 - S_{22}) - S_{12}S_{21}} \tag{3.9}$$

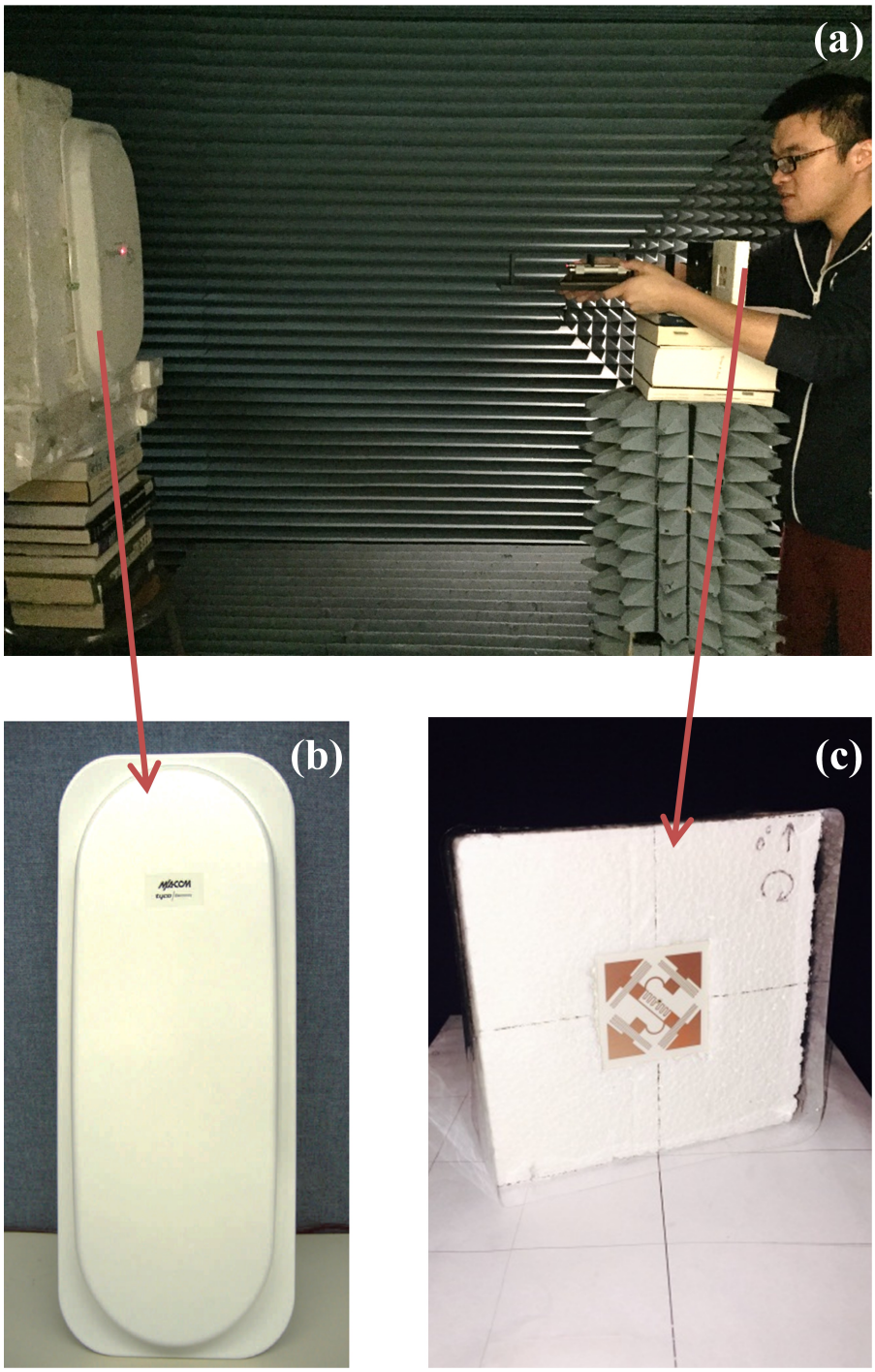

Figure 3.12: RFID tag antenna range measurement setup in the UCLA Antenna Lab. (a) System setup with (b) reader antenna and (c) tag antenna perfectly aligned.

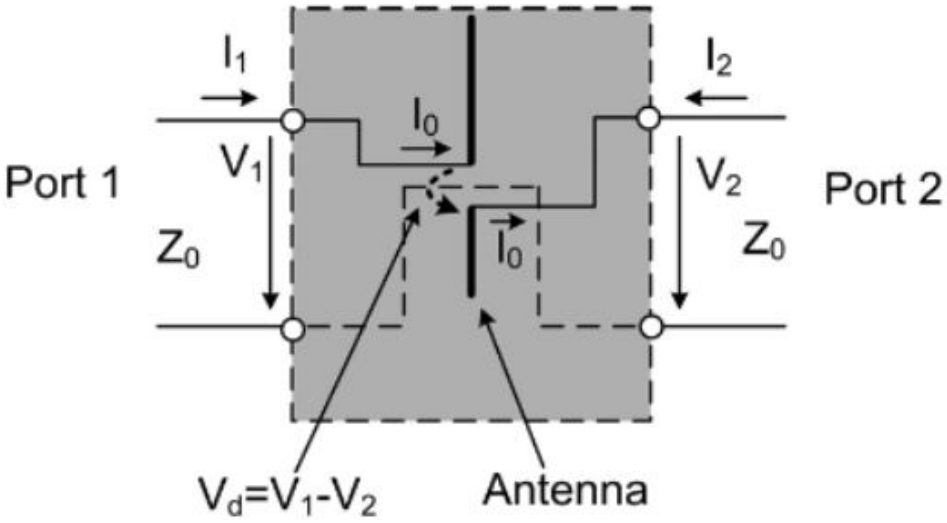

Figure 3.13: Network representation of the balanced antenna [38].

where Z_0 is the characteristic impedance of the connected coaxial cable which is typically 50 Ω. For symmetric antenna structures with $S_{12} = S_{21}$, the expression can be further simplified as:

$$Z_d = \frac{2Z_0(1 - S_{11}^2 + S_{12}^2 - 2S_{12})}{(1 - S_{11})^2 - S_{12}^2} \tag{3.10}$$

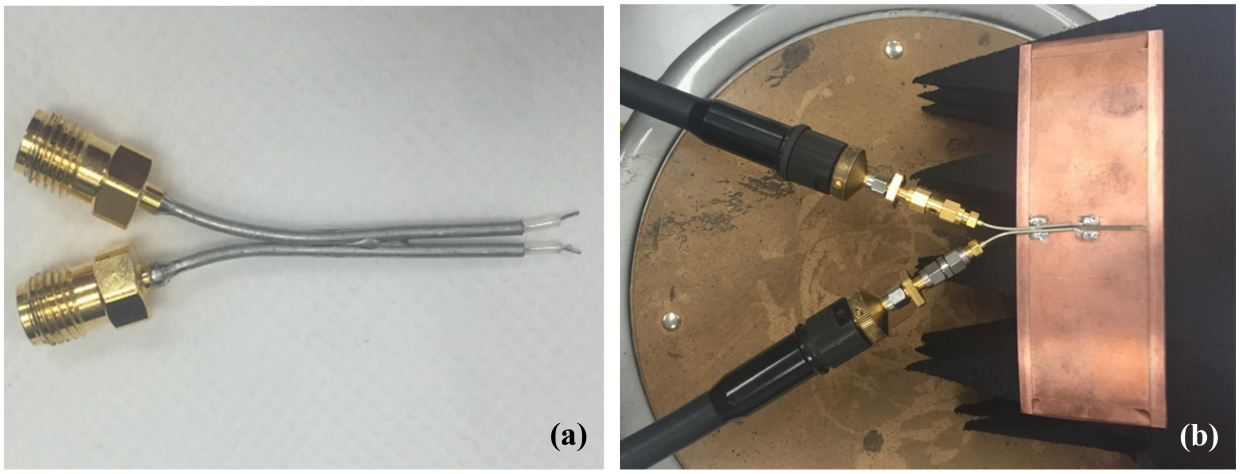

Figure 3.14: Setup for balanced antenna impedance measurement. (a)Fixture consists of two semi-rigid coaxial cables. (b)The balanced tag is connected to the 2 port VNA through the test fixture.

The setup of measurement system is illustrated by Fig. 3.14. The measurement is conducted by using a two-port VNA with port-extension functionality. A test fixture is constructed by two semi-ridge coaxial cables with one end connected to SMA connector and the other end open with small tip of inner conductor to connect with the antenna under test (AUT). The coaxial cables are soldered together on their outer conductors.

The measurement started with conducting standard VNA parameters setting and 2-port calibration (open, short, load and through). After calibration, the port extension was conducted to shift the calibration plane to take the length of text fixture into account. Note that the port extension only requires the test fixture to be connected to the test cables with tips open or short, that is, without loading the AUT. Here the short option was chosen since the perfect open is difficult to realize while simply solder the two tips together makes an almost perfect short. After port extension, the AUT was connected to the test fixture through the tips. Two-port S parameters were easily extracted and the impedance of AUT was calculated based on (3.9) for asymmetric AUT or (3.10) for symmetric AUT (see the MATLAB code in Appendix C).

3.6 Measurement Results and Discussion

The CP and LP antennas were fabricated on Rogers RO4003 laminate with thickness of 31 mil. The Monza 5 chips and NXP G2XM chips with Cu straps were integrated to the fabricated antennas using conductive epoxy, as shown in Fig. 3.15 and 3.16.

The read range of the antenna prototypes were measured in an anechoic chamber. The RFID reader and reader antenna are specified in previous discussions. During the first measurement, the tag antenna was placed at a fixed position 40 cm away from the reader antenna and the minimum transmitting power required to activate and read from the tag was recorded.

Several observations can be made from the results listed in Table 3.8. First, the tags integrated with NXP chips had significantly better performance compared to those mounted with Monza5 chips, even though the read sensitivity of NXP chip (-15 dBm) is 2.8 dBm lower

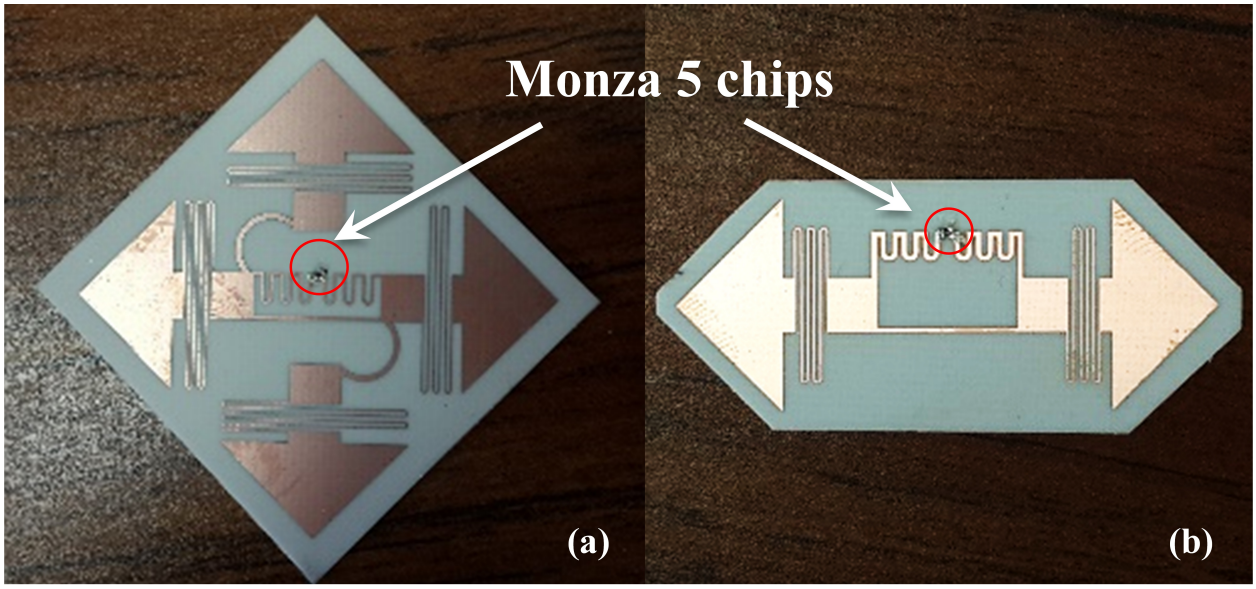

Figure 3.15: Fabricated meandered RFID tag antenna prototypes with Monza5 chips. (a) CP cross-dipole and (b) LP dipole prototypes.

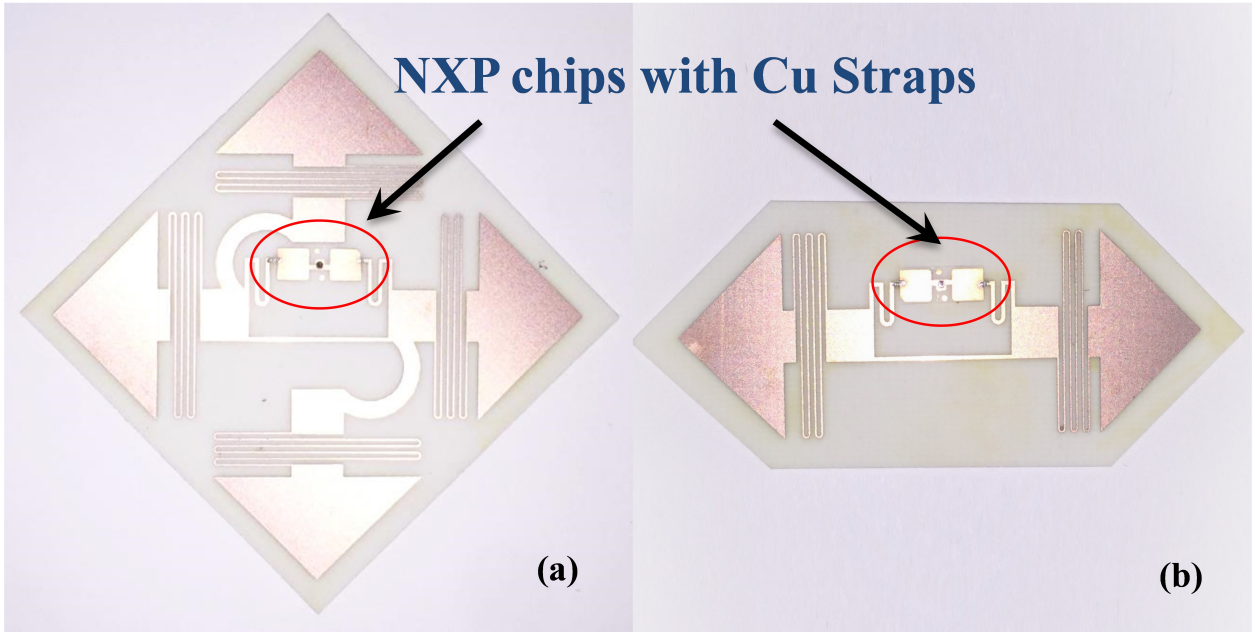

Figure 3.16: Fabricated meandered RFID tag antenna prototypes with NXP chips with Cu straps. (a) CP cross-dipole and (b) LP dipole prototypes.

than the sensitivity of Monza5 chip (-17.8 dBm). This could be explained by the effects of Cu straps on the package of NXP chips, which gives more reliable connection between chip pads and antenna ports, and thus enhances impedance matching. Second, for the tags with NXP chips mounted on, a 2 dBm sensitivity enhancement was observed for the CP tag compared with the LP counterpart. This is not as high as the theoretical improvement of 3 dB from LP to CP. However, as we refer to the AR simulation shown in Fig. 3.8 and the plot in Fig. 3.17 for the theoretical sensitivity improvement versus AR based on link budget calculation, a 2 dB sensitivity enhancement is exactly matched with the 2.5 dB AR from simulation. Third, since our connections with Monza5 are doubted, we compared the measurement results with a commercially built Monza5 LP RFID tag with similar dimensions as our design. Note that Monza5 chips are 2.8 dB more sensitive than NXP chip, and with that taken into account, the performance of our LP antenna is comparable with commercial LP tag antenna, and our CP antenna gives a 2 dB sensitivity enhancement compared to the commercial one.

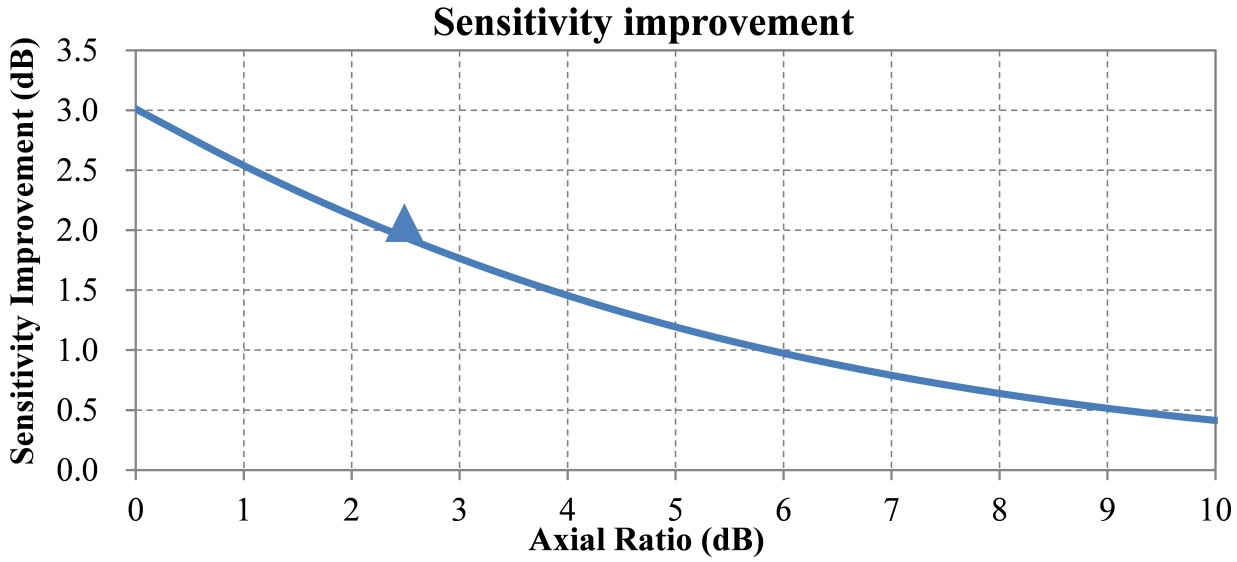

Figure 3.17: Improvement of sensitivity from LP to CP with varying AR.

A second measurement was carried out to study the effects of angular rotation and tilting to the CP antenna performance. During the second measurement, the tag antenna was again placed at a fixed position 40 cm away from the reader antenna and was tilted or rotated by a certain angle, as illustrated in Fig. 3.18 and 3.19. The minimum transmitting power

Table 3.8: Measurement results of minimum activate power at d = 40 cm.

Tag under test	LP tag (NXP)	CP tag (NXP)	LP tag (Monza5)	CP tag (Monza5)	Commercial tag (Monza5)
P_{min}	18 dBm	16 dBm	18 dBm	23 dBm	15 dBm

required to read from the tag was recorded, as listed in Table 3.9.

Table 3.9: Measurement results of minimum activate power at d = 40 cm as the CP tag was rotated and tilted.

Rotation Angle	0°	90°	180°	270°
P_{min}	16 dBm	16 dBm	16 dBm	16 dBm
Tilting Angle	30°	-30°	90°	-90°
P_{min}	18 dBm	18 dBm	20 dBm	20 dBm

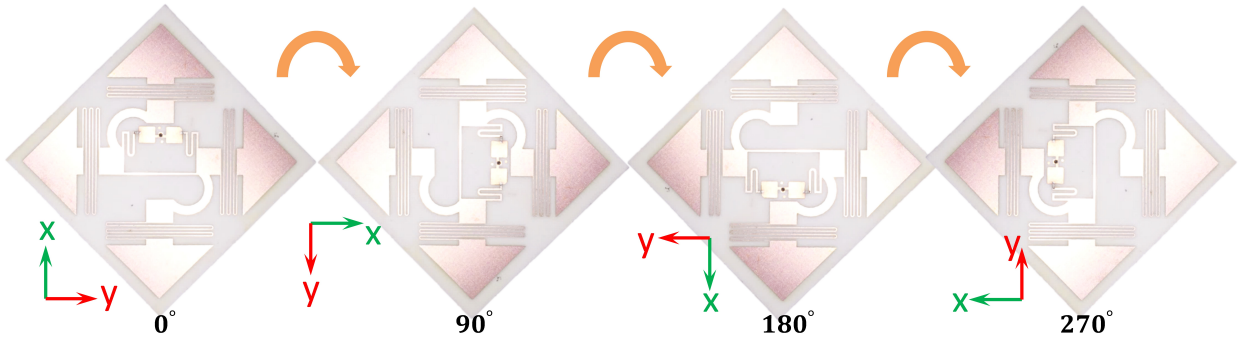

Figure 3.18: Rotating the NXP CP tag antenna for 0°, 90°, 180° and 270°.

The results from the second measurement confirms that rotation does not affect the performance of CP antenna, while tilting could affect the sensitivity for up to 4 dB, which matches with the radiation pattern expected by simulation results in Fig. 3.9. The simulated total gain decreases by 1.5 dB for 30° tilting and 3.5 dB for 90° tilting, while the measured sensitivity decrease are 2 dB and 4 dB, respectively.

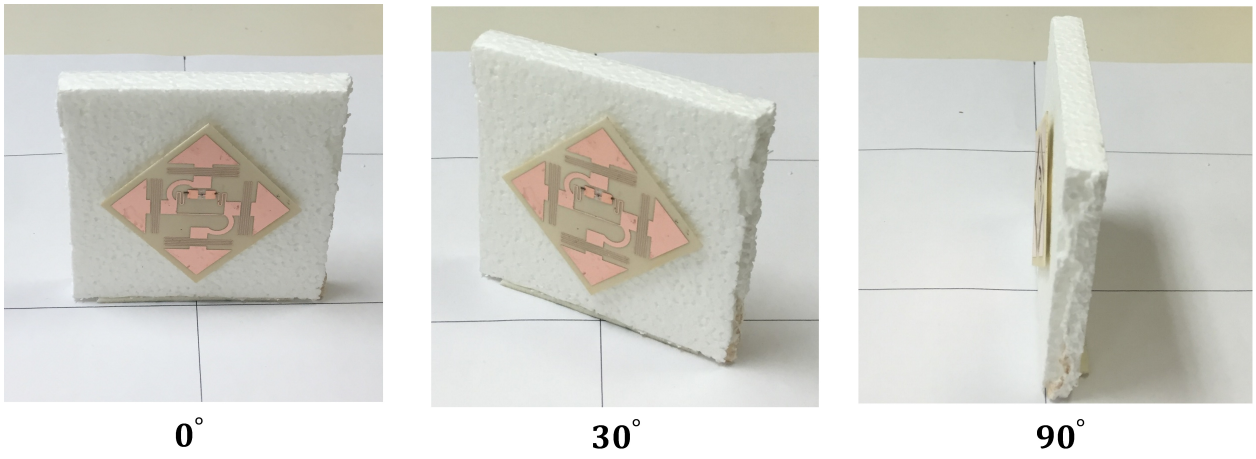

Figure 3.19: Tilting the NXP CP tag antenna for 30°, -30°, 90° and -90°.

CHAPTER 4

System Architecture of Antennas for Wireless Brain-Machine Interfaces

Brain-machine interface (BMI) technology is a new and multidisciplinary field that holds great potential for patients suffering from a wide variety of severe neurological conditions, such as paralysis, stroke, and spinal cord injury [40]. Impressive growth has occurred in this field through decades since the first experimental demonstration that electrical activity generated by cortical neurons can be extracted and applied to control robotic manipulator [41]. The research goals on BMI systems are to record neural data and transform thought into action, which fulfill the dream of many patients living independently, using prosthetic limbs in the same way as biological ones. Such systems require multichannel sensors for neural recording, specialized IC for signal processing, programs for brain simulation, a wireless link to communicate with external unit, and finally a real-time mechanical actuator to control a three-dimensional prosthetic limb.

Currently, two main challenges remains in the development of reliable and long-lasting BMI systems. One is to control a multi-degree-of-freedom artificial limb in a manner comparable to natural movements [42], and the other is to build viable neural interfaces that last a lifetime. A long-lasting neural interface should be biocompatible and extremely small, to minimize tissue damage. The neural implant should thus be wirelessly powered, require minimum power, and support bidirectional data flow, i.e., reading and writing from or to the brain. Study of the wireless data and power transmission technique plays a key role in this endeavor.

This chapter discusses the system architecture of miniature telemetry antennas used for

wireless power and data transfer in BMI systems. We start with an overview of the state-of-the-art BMIs, followed by specified antenna design criteria for such applications. Then we introduce the mechanism of wireless power and data transfer of biomedical implants, and finally come to the detailed analysis of transmitting and implanted antennas.

4.1 Overview of Wireless Brain-Machine Interface Systems

4.1.1 Neural Signals and Neural Recording

When it comes to recording neural signals, different methods exist, depending on the level of invasiveness and the required spatial resolution [18]. Typically more invasive recording method gives signal with better quality. This section briefly introduces the popular neural recording methods and their applications.

The most non-invasive and convenient method is based on electroencephalograms (EEGs), in which neural signals are acquired by placing sensing electrodes on the top skin of the head. EEGs records signals that represent the superimpose of the electrical activity generated by a large number of neurons close to the recoding position and thus suffer from low spatial and temporal resolution. Accordingly, BMIs based on EEGs are used for simple task, such as controlling a computer cursor or operating a wheel chair.

A more invasive method called electrocorticography (ECoG) uses electrodes implanted on surface of the cortex. ECoG compared with EEG allows recording from a more localized area (i.e., 10s of mm vs. cm), with broader bandwidth (i.e., 0-500 Hz vs. 0-50 Hz), and higher characteristic amplitude (i.e., 50-100 μV vs. 10-20 μV) [43]. However it's still not good enough to acquire signals for complex task such as the multi-degree movement of artificial limb, which requires methods with better resolution.

The most invasive yet most accurate method uses microelectrodes to acquire the local activity of neuron. In this method, electrodes with diameters of a few 10s of μm penetrate the cortex for 100s of μm to get signals. Obviously such an approach is much more invasive than EEGs or ECoG, but the increased signal fidelity outweighs the risks in many cases.

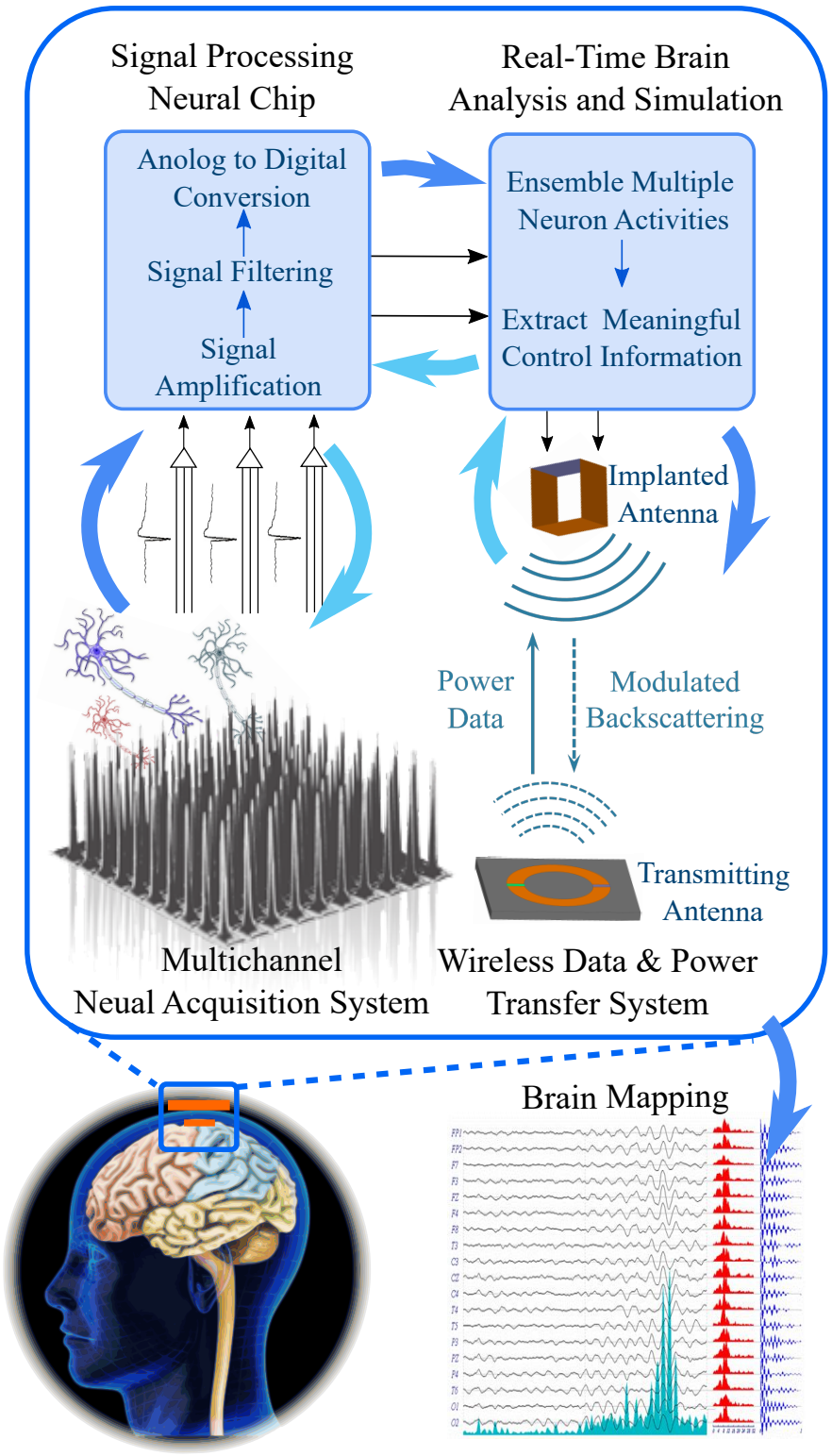

Figure 4.1: Schematics illustration of a general BMI system architecture.

Therefore the reminder of the thesis focus on system development based on this method.

Microelectrodes implanted introcranially typically record neural signal as a combination of the local field potential (LFP), action potential (AP) or spikes, and a DC offset due to electrochemical interfacing. The AP signals contain information from 300 Hz to 10 kHz generated from a single neuron, while the LFP signals are typically below 300 Hz, in the form of "brain waves".

However, one of the existing problems associates with microelectrode arrays is the difficulty to record signals stably over long time [44, 45]. Experiments showed that, a few days after implantation, the human body starts forming scarring tissue (Fig. 4.2), which gets in between the recording site of the electrode and the neurons. As a result, the signal-to-noise ratio (SNR) of the recorded signals degrades over time and eventually becomes too low to extract reliable information. A number of research projects focus on overcoming this problem, including approaches investigating different materials and/or shapes of electrodes or improving the surgical procedures to implant the electrodes.

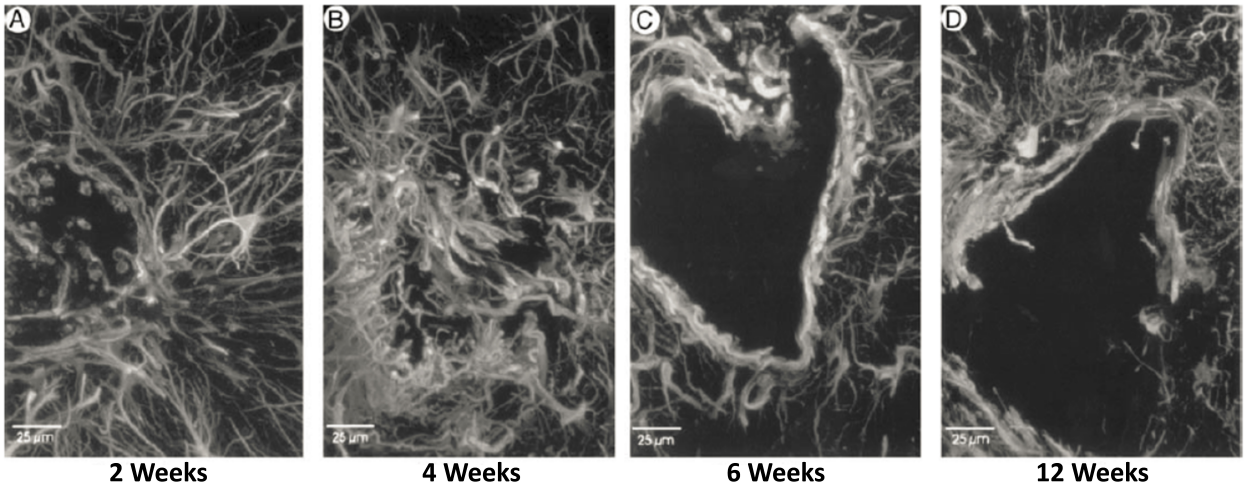

Figure 4.2: Tissue response to microelectrodes over time [44].

4.1.2 BMIs: Past, Present and Future

Research on BMIs has grown in a stunning pace since the first experimental demonstration by Eberhard in 1999 that ensembles of cortical neurons could directly control an actuator (Fig. 4.3) [41]. Since then people have done a lot of works on this topic and many interesting demonstrations have been set up. Many of them using non-invasive method exploiting electroencephalograms (EEGs). However since the neural signals severely attenuate through transmission in head tissue, and signals generated from different neurons interfere and superimpose with each other, the non-invasive method is very limited in spatial resolution, which makes them difficult to complete complex task, such as movements of artificial limbs with multi-degree of freedom. In comparison, invasive BMIs use electrodes implanted intracranially to acquire raw brain activities . This method apparently carries risks associated with surgeries. Yet it provides signals with good quality regarding spatial resolution and bandwidth.

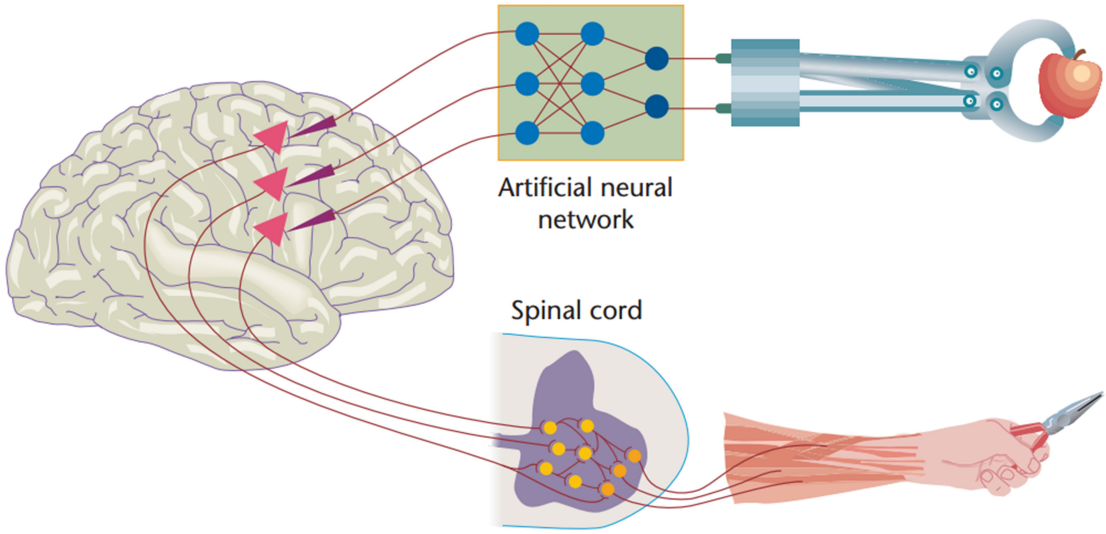

Figure 4.3: The first experimental demonstration in 1999 that ensembles of cortical neurons could control an actuator [41].

BMI technology holds promise to revolutionize modern health care. However, bottlenecks still exist that preclude BMIs from clinical application. For example researchers are still working on stable and long-term recordings of large numbers of neurons (i.e. hundreds to

thousands) from multiple brain areas [40]. Most of existing state-of-art systems are based on wired data transfer, which limits the freedom of patient and increase the risk of injury and infection.

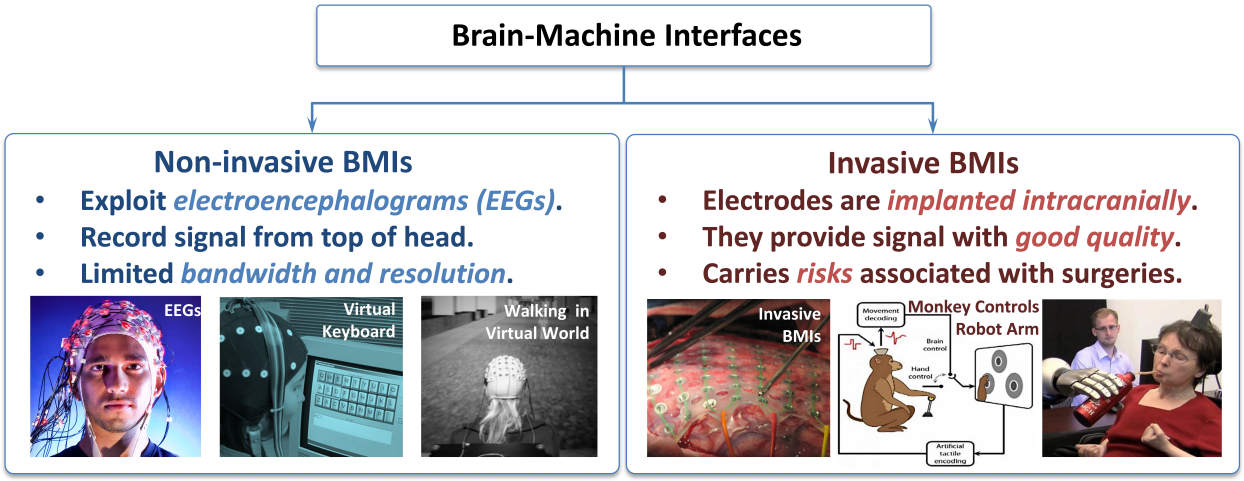

Figure 4.4: Classifications of the existing brain-machine interfaces [46–50].

4.1.3 Proposed Antenna System for BMIs

Addressing the above requirement, we need to design miniature antenna system that can support wireless data flow. And in order to support multi-channel multi-area neural recording and high data rate, the antenna system should have a reasonable bandwidth. Also to achieve fully passive system, the wireless link should be able to transfer power efficiently in human tissue. And finally, the specific absorption rate should be compliant to FCC regulation, which means the maximum SAR generated in tissue should be less than 1.6 W/kg [51]. And that limitation defines the maximum power level that can be safely transferred in skin.

4.2 Wireless Power and Data Transmission

When it comes to wireless power and data transfer, it is critical to have a good understanding of the wireless channel. In the case of wireless transfer to biomedical implanted devices, the

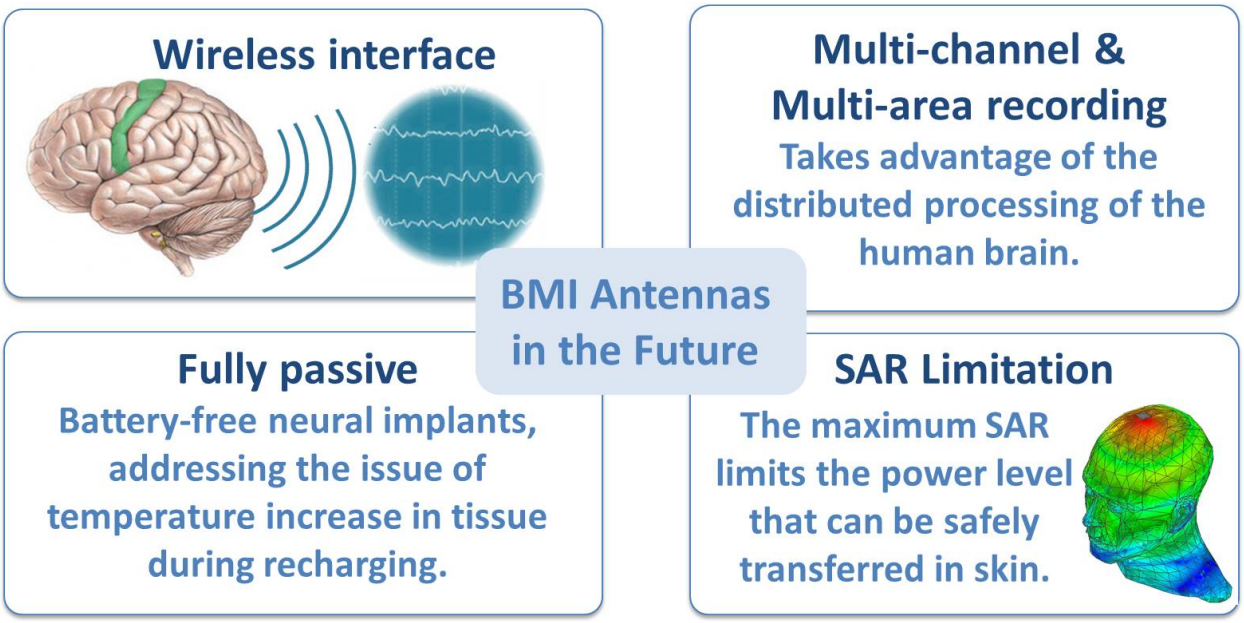

Figure 4.5: Antenna design challenges: fully passive, integrated, and ultra low power wireless neural interfaces

channel consists of layers of various kinds of tissues such as skin, fat, dura etc., each having unique dielectric and loss properties [27, 52]. In order to find the optimum link parameters such as frequency of operation and antenna geometries, Thus, full-wave electromagnetic simulations are required in order to find the link parameters that optimize the overall power and data transfer efficiency through the region of operation . Using good models for the tissue parameters is crucial for the accuracy of the simulations.

In this work we focus on antennas for invasive BMI systems with a miniature neural recording system implanted in CSF fluid on top of the brain, and a transmitting device sitting on top of the skin that generates the near-field electromagnetic field to power the implanted device, as shown in Fig. 4.6. The transmitting antenna is interfaced with a power and data telemetry similar to an RFID reader. And the implanted antenna is connected to a neural recording IC similar to the RFID tag chip. The external device is not constrained in size to the first order, but is desirable to be low-profile and wearable in order to be easily integrated into cloth or head stage. The main challenge is the requirement of minimized space as well as the difficulty of getting access to the device once it is implanted by surgery.

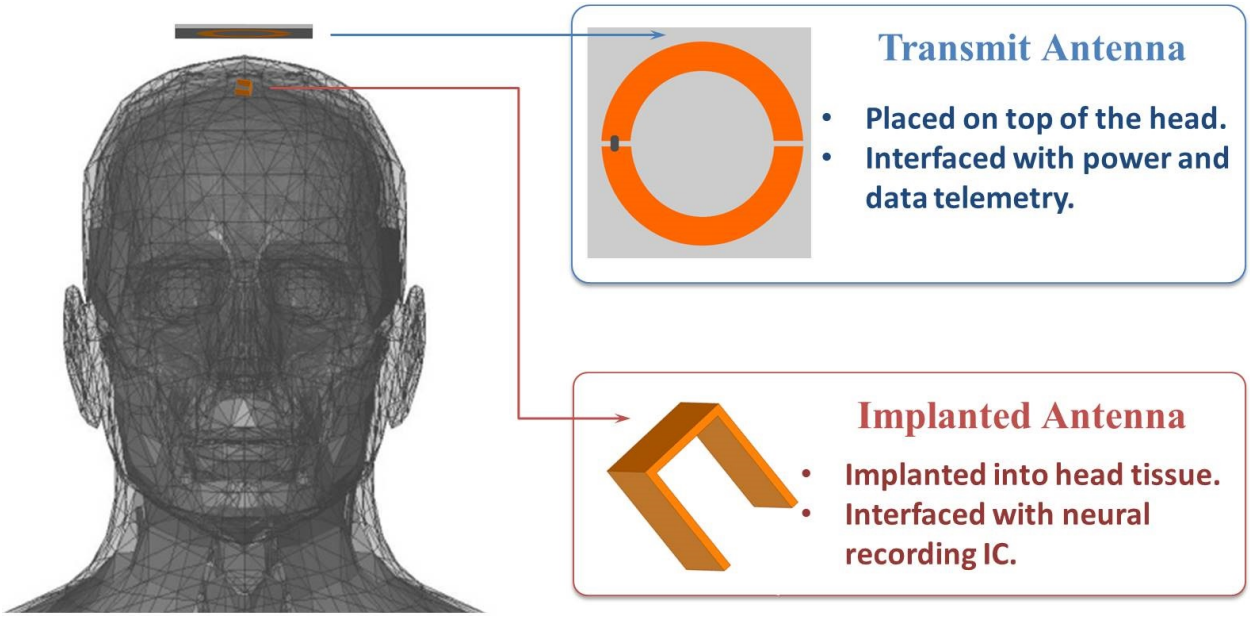

Figure 4.6: Antenna system setup: implanted antenna and transmitting antenna.

The channel itself consists of various types of tissue and can be modeled as layers of bone, fat, skin etc.. Depending on the age of the patient and due to variations in anatomy the different layers can add up to a total of between 1 and 10 mm [53]. In the rest of the work we consider the general case of 5 mm distance from top skin to implant cite. The dielectric properties of the different types of tissue were modeled in the finite element based electromagnetic field solver (ANSYS HFSS) to simulate the overall link efficiency.

Due to the size and power constraints, mm-size implanted wireless devices can only operate over a short distance of a few millimeters, and thus mainly operate in the near-field region. Considering the fact that human tissues absorb electric field but conducts magnetic field, magnetic antennas with low electric near fields are the preferred candidates for antennas for biomedical implants. Loop antennas generate small electric near fields while providing rather strong near-field magnetic field and efficient inductive coupling and are therefore commonly used for wireless implants.

Considering the above-mentioned system requirements and limitations, short-range RFID backscattering technology might be one of the most promising and safest methods for estab-

lishing wireless powering of and communicating with miniature neural implants. In such a system, power and data transfer is achieved by near field inductive coupling between transmitting antenna and implanted antenna [54]. The power received by the implanted antenna will activate the neural recording IC. Just like the operating mechanism of any passive RFID tags, the data link is established through the modulation of the impedance at the terminal of the implant antenna according to the acquired neural signal [21]. The complexity is thus predominantly at the external transmitter or interrogator, which enables the neural implants to be designed fully passive with ultra-low power consumption, resembling to RFID tags. The operating mechanism is illustrated in Fig. 4.7.

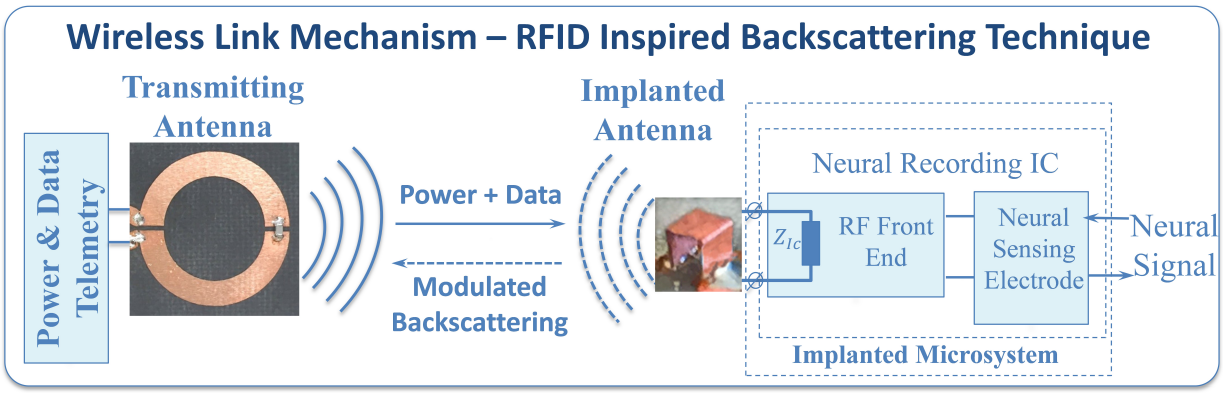

Figure 4.7: Wireless link mechanism: RFID inspired backscattering technique.

4.3 Characterization of Wireless Channel

Power is transferred from outside to the implants by short-range backscattering technology using near-field inductive links with loop antennas, which is a desirable method to transfer power efficiently through short distances and highly dissipative media, such as human head. A wireless inductive link between transmitting and implanted loop antennas can be characterized as a linear microwave two-port network as shown in Fig. 4.8, since antennas have an influence on each other in a near-field wireless system.

For a two-port network, input and output impedances are related to the source and load

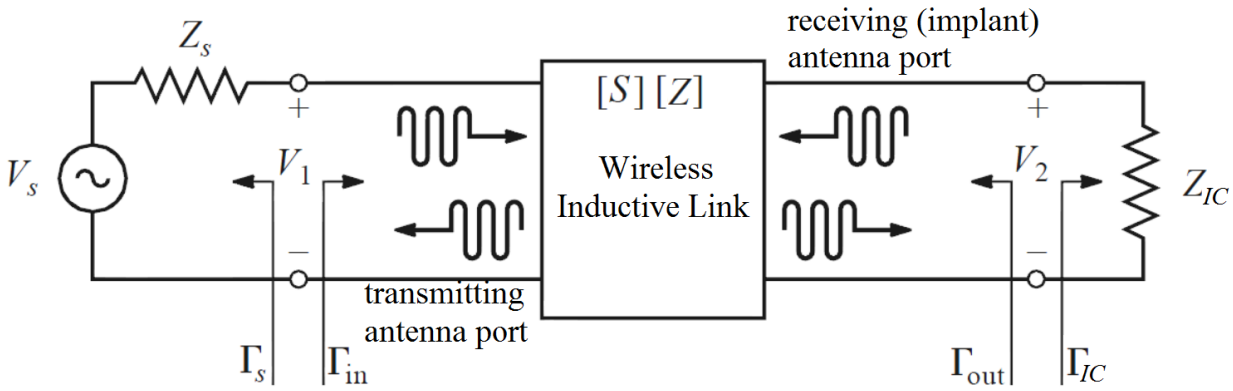

Figure 4.8: The wireless channel modeled as a linear two-port network.

impedances and two-port Z parameters as [39]:

$$Z_{ta} = Z_{in} = Z_{11} - \frac{Z_{12}Z_{21}}{Z_{22} + Z_{IC}} \tag{4.1}$$

$$Z_{ra} = Z_{out} = Z_{22} - \frac{Z_{12}Z_{21}}{Z_{11} + Z_s} \tag{4.2}$$

The effective coupling between antennas can be described by link power efficiency $G_{p,max}$, which is defined by the maximum ratio of the power delivered to the implanted microsystem to the power supplied to the external transmitting antenna, achieved as the delivered power at the two ports are maximized and the ports are simultaneously conjugate matched:

$$Z_{ta} = Z_s^*, Z_{ra} = Z_{IC}^* \tag{4.3}$$

In the case of near-field coupling between loop antennas, the link power efficiency $G_{p,max}$ is represented in terms of the two-port S parameters as [28]:

$$G_{p,max} = \frac{P_{IC}}{P_{avs}} = K - \sqrt{K^2 - 1}, where \tag{4.4}$$

$$K = \frac{1 - |S_{11}|^2 - |S_{22}|^2 + |S_{11}S_{22} - S_{12}S_{21}|^2}{2|S_{12}S_{21}|} \tag{4.5}$$

Based on the two-port Z parameters the link power gain can also be written as:

$$G_{p,max} = \frac{|Z_{21}|^2}{S + \sqrt{S^2 + |Z_{12}Z_{21}|^2}}, where \tag{4.6}$$

$$S = 2Re(Z_{11})Re(Z_{22}) - Re(Z_{12}Z_{21}) \tag{4.7}$$

where the subscript 1 refers to transmitting port and subscript 2 refers to implanted port.

For wireless devices transmitting power toward the human body, the exposure of the tissues to the electromagnetic field need to be taken into consideration. According to FCC regulations, the maximum specific absorption rate (SAR) level generated in tissue should be less than 1.6 W/kg, which limits the maximum amount of power that can be safely delivered by the transmitting antenna:

$$P_{t,max} = \frac{(1.6W/kg)\tau_s}{SAR_{max}} P_t \tag{4.8}$$

Here, P_t is the assigned test power in simulation model and τ_s is the ratio of the power available to the transmitting antenna port to the power delivered from the source. Thus, the maximum power available to the implant device is simply defined as:

$$P_{L,max} = G_{p,max} P_{t,max} \tag{4.9}$$

The goal of telemetry antenna design is to maximize the available power P_L, by maximizing both the link power efficiency and the maximum transmitting power.

4.4 Transmitting Antenna Design

On the transmitting antenna side, the goal is to design transmitting loop that provides high inductive coupling with the implanted loop to maximize the link power efficiency, as well as low SAR to enhance the maximum SAR compliant transmit power. The design criteria can thus be summarized as:

1). High near magnetic field and efficient coupling with implanted antenna.

2). Low near electric field, since the local SAR is proportional to the square of the magnitude of the electric field.

3). Low profile design, since the ultimately the transmitting antenna should be fabricated as part of the clothing-integrated and wearable device.

4.4.1 Optimized Transmitting Antenna Dimensions

For the application of BMIs, the implanted antenna is constrained in size while the transmitting antenna can be designed larger to enhance the coupling efficiency. We therefore start by fixing the size constrained implanted antenna when optimizing the overall link. In the following discussion the size of implanted antenna is constrained to 1 mm^3 with 0.03 mm thickness. Prior research have reported that the frequency with minimized link loss shifts down to lower frequencies and the minimum link loss decreases with increasing transmitting antenna size [55, 56]. Accordingly there should exist a optimized size for minimum link loss and hence maximum the overall link efficiency for an assigned frequency of operation . In this study the optimum size for inductive loop antenna is represented by its radius, with the trace width fixed to 3 mm through the study to lower ohmic loss. In order to investigate the changing of optimum loop size with frequencies, we modeled the links with transmitting antennas of varying inner radius over a frequency range of 300 MHz to 500 MHz, as shown in Fig. 4.9.

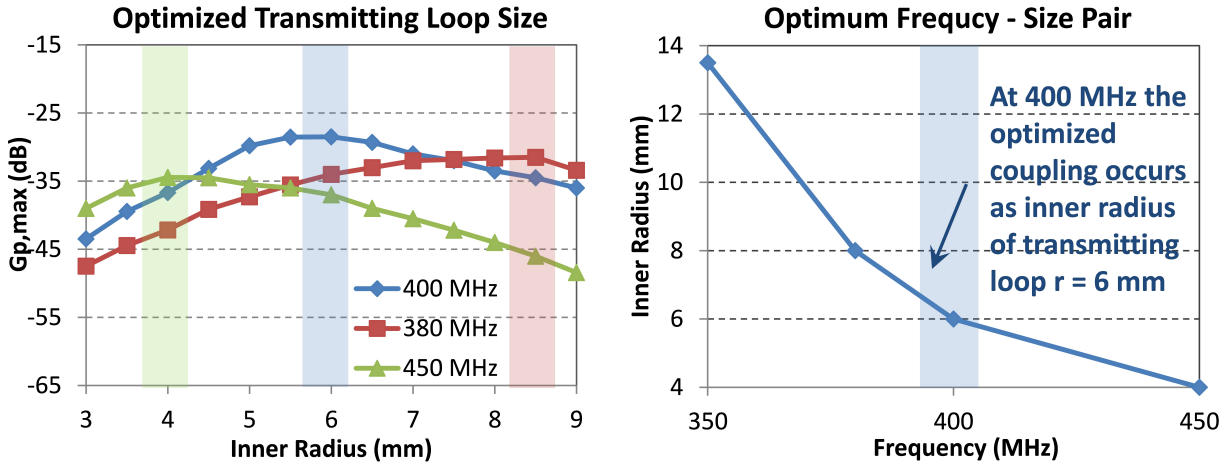

Figure 4.9: Simulated link efficiency with varying inner radius at different frequencies.

According to the results for antennas operating at 350, 400, 450 MHz, the optimum transmitting antenna size exist for an assigned frequency and a given receiving antenna [57]. The optimum transmitting antenna size increases at lower frequency and decreases at higher

frequency. We can also observe that at our frequency of interest around 400 MHz the corresponding optimum transmitting antenna size coupling with a 1 mm^3 receiving antenna is 6 mm in inner radius. For this particular optimum antenna configuration, the link power efficiency has a peak of around -27 dB, which is commonly accepted as was discussed in [20].

In this simulation the separation between loop antennas are set as 15 mm, which is on the same order as the dimensions of the transmitting antenna with the optimum size observed here. The implanted antenna is thus operating in the source region of the transmitting antenna, and none of the common near or far field equations are applicable in this region [58]. Therefore it is necessary to apply full wave simulation to analysis the link performance even through we are using rather simple antenna configurations.

4.4.2 SAR Reduction

By applying the optimum configurations given by the previous section, we can easily obtain a planar transmitting antenna with copper printed on substrate. However, the problem associated with the solid loop structures is the E field hot spots generated in the region close to the feeding point. This is due to the fact that for a few 100 MHz carrier frequencies, the current distribution within the loop is nonuniform, and therefore E field hot spots appeared on the skin when the transmitting loop was brought near the skin [20, 59]. The presence of E field hot spots leads high local SAR, which is undesired since it would strongly decreases the maximum allowed transmit power.

Prior research has demonstrated that by partitioning the transmitting loop into segments and inserting capacitors within the gaps, current continuity and uniformity can be enhanced and E field hot spots in human tissue can be averaged effectively [60]. The capacitors were to be chosen to resonant with the loop inductance and to compensate for the phase shift along the loop due to its dimension. The effect of segmenting planar loop structure to reduce local SAR is illustrated by simulation results of E field and H field shown in Fig. 4.11.

It might be tempting to do more segmentations based on the simulations. For real implementation however, the use of lumped capacitors would introduce parasitic loss and

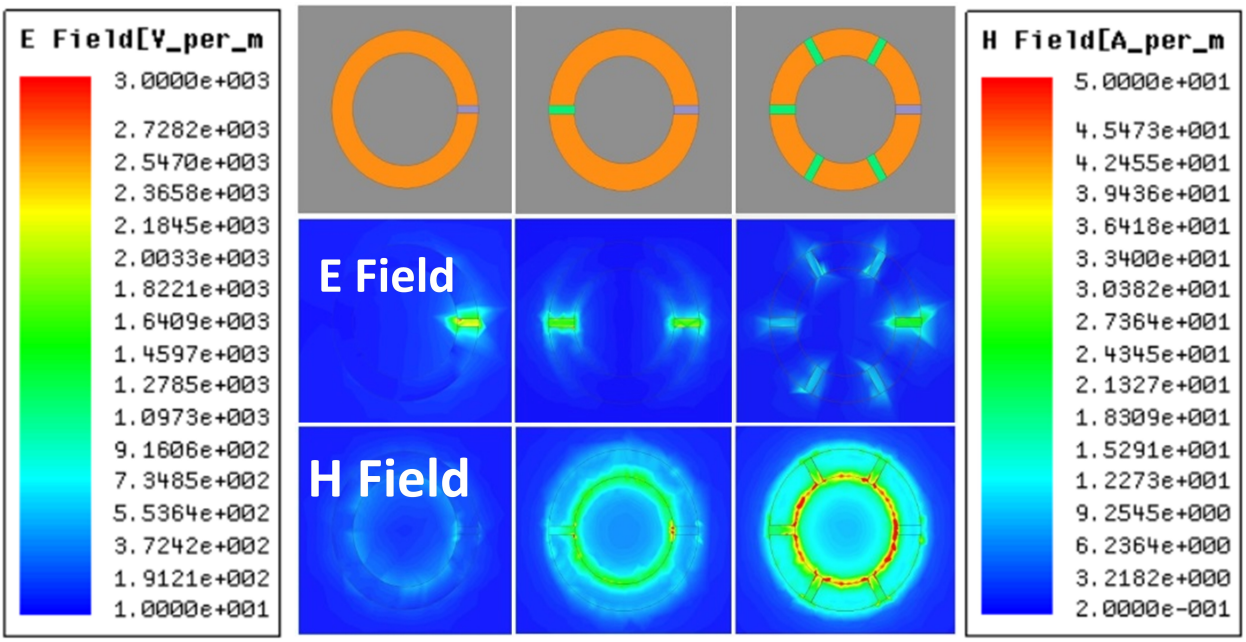

Figure 4.10: Segmenting the loop antennas and inserting serial capacitors to average electric field hot spot and enhance coupling.

thus decrease the overall link power efficiency. Therefore, in this study, we use a 2-segmented planar copper loop structure for transmitting antenna and connect the segments with 36 pF capacitor. The 2-segmented loop can thus achieve a similar link efficiency as the solid loop and provide a lower local SAR at the same time. As shown in Fig. 4.10, antenna was simulated and fabricated on a 31 mil Rogers RT/Duroid 5880 substrate (ϵ_r=2.20) with 6 mm inner radius and 3 mm trace width, which are the optimized size according to previous section with maximum coupling with the fixed implanted loop at the MICS frequency band of 402-405 MHz.

4.5 Implanted Antenna Design

The implantable antenna should be bio-compatible and miniaturized without increasing the size of the implanted system significantly. Thus, ultra-compact antennas are desirable solutions for localized neural recording systems. Here we used 1 mm^3 3D cubic loops in

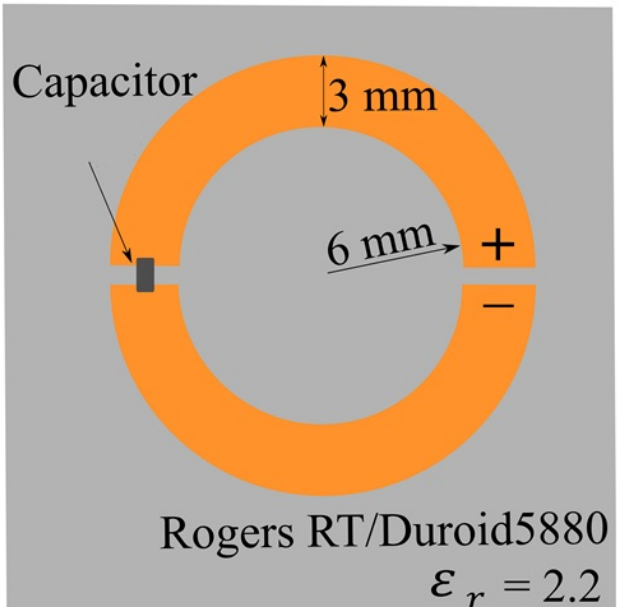

Figure 4.11: Segmenting the loop antennas and inserting serial capacitors to average electric field hot spot and enhance coupling.

copper (Fig. 4.12), which provides wider current path and larger coupling area compared to their planar counterparts with the same cross-section area. Moreover, the cubic structure allows for the insertion of a magnetic core to further enhance the inductive coupling.

The implanted small loop antenna was designed to be interfaced with a miniature neural recording IC implanted in the CSF fluid on top of the back of the microelectrode array, which sits on top of the cortex and connected to the neural recording system by wires.

In this section we discuss the optimum small loop dimensions to further enhance coupling, and then compare the link efficiency using the cubic loop and wired loops. We stick on the transmitting loop antenna design given by the analysis in the previous section.

4.5.1 Optimized Implanted Antenna Dimensions

For a given transmitting antenna and assigned frequency, the optimum implanted antenna size can be easily found as discussed in the previous section. However, for the application of implanted neural sensing microsystem, the occupied space of antenna is a major design

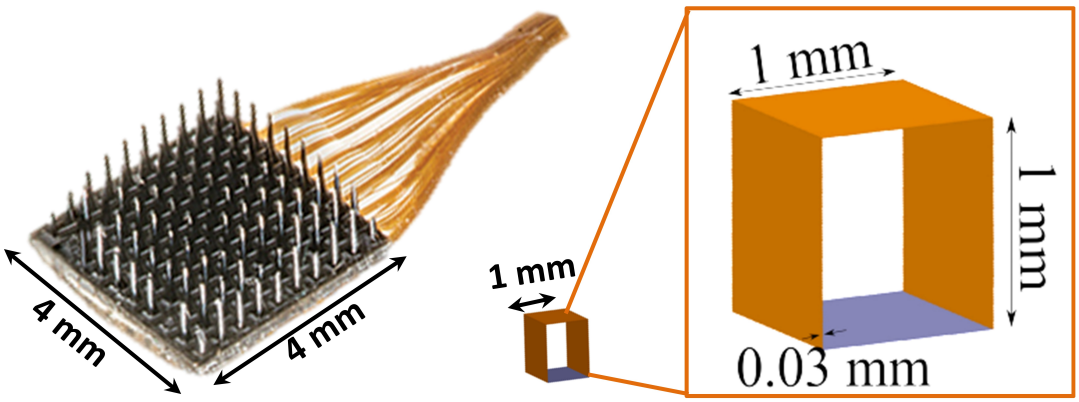

Figure 4.12: Millimeter size cubic loop antenna compared with typical neural recording electrode array [61].

constraint. We therefore started with millimeter-size small loop and investigate how the optimum values for the link change for different implant sizes, simulation similar to the one for transmitting antenna was carried out, as shown in Fig. 4.13. The implanted antenna is modeled as cubic loop antenna with its dimension varying between 0.5 and 10 mm. The optimum frequency with the maximum coupling increases with decreasing size, starting at a few 10s of MHz going all the way up to a few 100s of MHz. We thus chose the size of implanted loop antenna with 1 mm dimension, with an associated optimum frequency of around 400 MHz.

Effect of copper thickness is studied by comparing two models with same outer dimensions but different in copper thickness (0.03 mm and 0.3 mm). Fig. 4.14 shows the simulated link power efficiency of the 1 mm^3 implanted loops coupling with the planar transmitting loop described in the former section. Again, the implanted loops were aligned at the lateral center of transmitting loop with vertical distance of 15 mm. We also observe a 2 dB enhancement in coupling efficiency of the link with 0.03 mm thick implanted loop, comparing with the 0.3 mm counterpart. Thus for the rest of this study we use the 0.03 mm copper foil for implanted antenna fabrication.

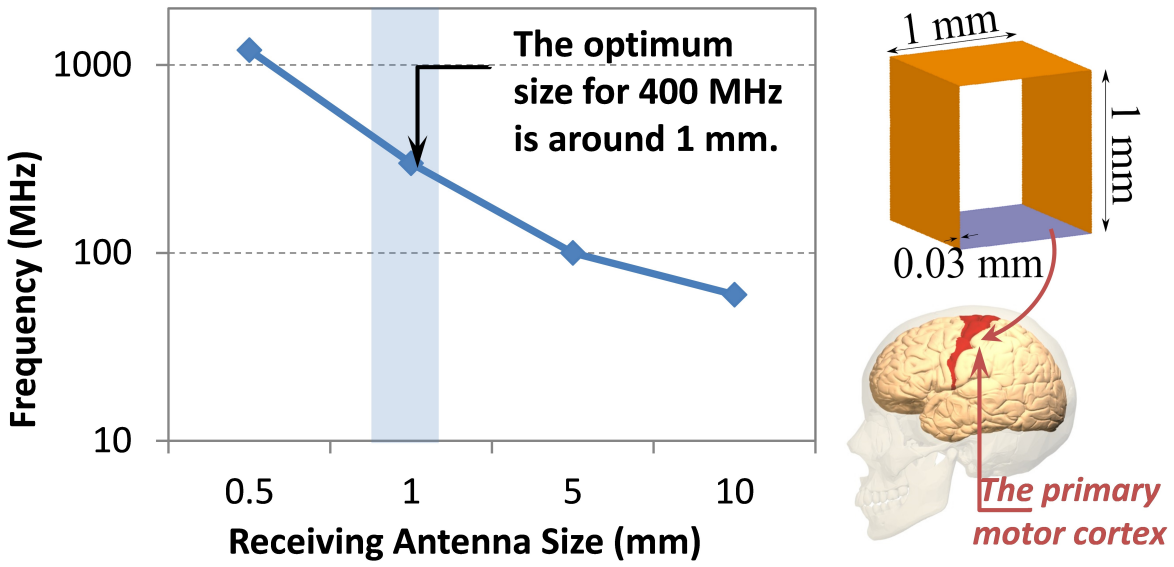

Figure 4.13: Millimeter size cubic loop antenna optimized for frequency of around 400 MHz, immersed inside CSF fluid in the primary motor cortex area.

4.5.2 Comparison of Cubic and Wire Antenna Structures

To investigate the advantages of using a cubic structure rather than coils, we compare the link efficiency of cubic loop structure and wire loops with single turn and multiple turns, as shown in Fig. 4.15. The wired loops are modeled with the same cross-section area as the cubic and the overall separation between feeding ends. Their occupied volume is thus about the same as cubic loop and the performance are comparable. Link efficiencies are simulated with the designed planer transmitting loop antenna.

Based on the simulation results, we can observe up to 25 dB coupling enhancement compared to single-turn loop and 10 dB enhancement as we increase the wire loop to 5 turns. As the number of turns increase, the multi-turn wire loop is approaching the solid 3D structure and showing reasonable performance. However considering the ease of fabrication, we still use the cubic loop structure in the following discussions.

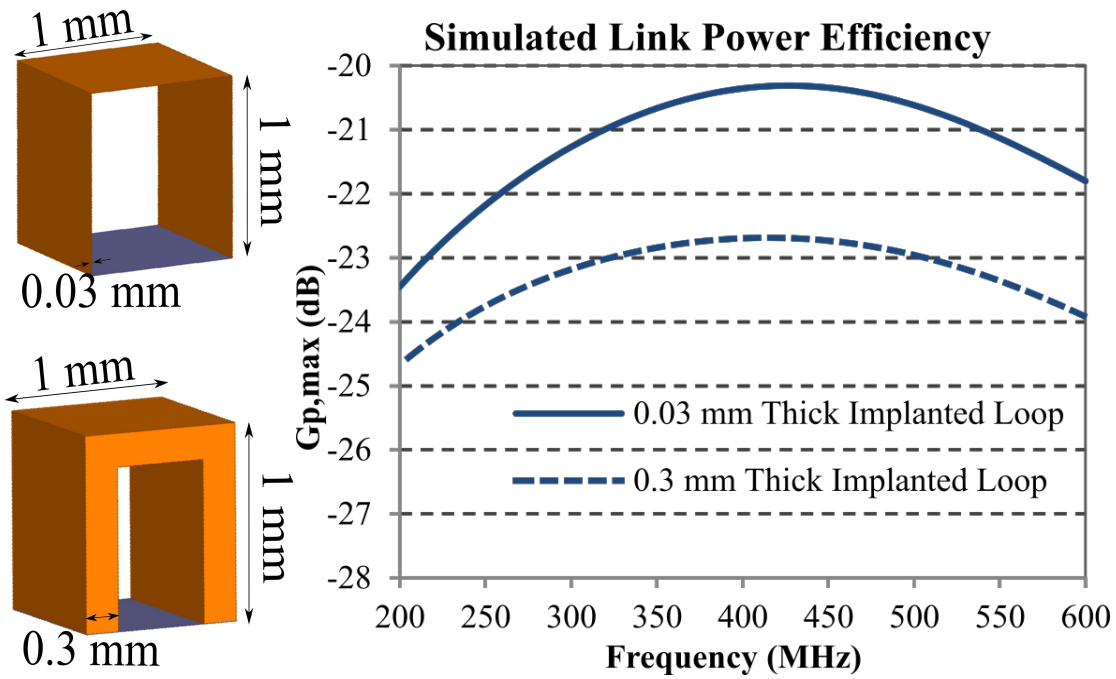

Figure 4.14: Simulated link power efficiency of implanted loop antennas (0.03 mm and 0.3 mm thickness) coupling with 2-segmented planar transmitting loop antenna.

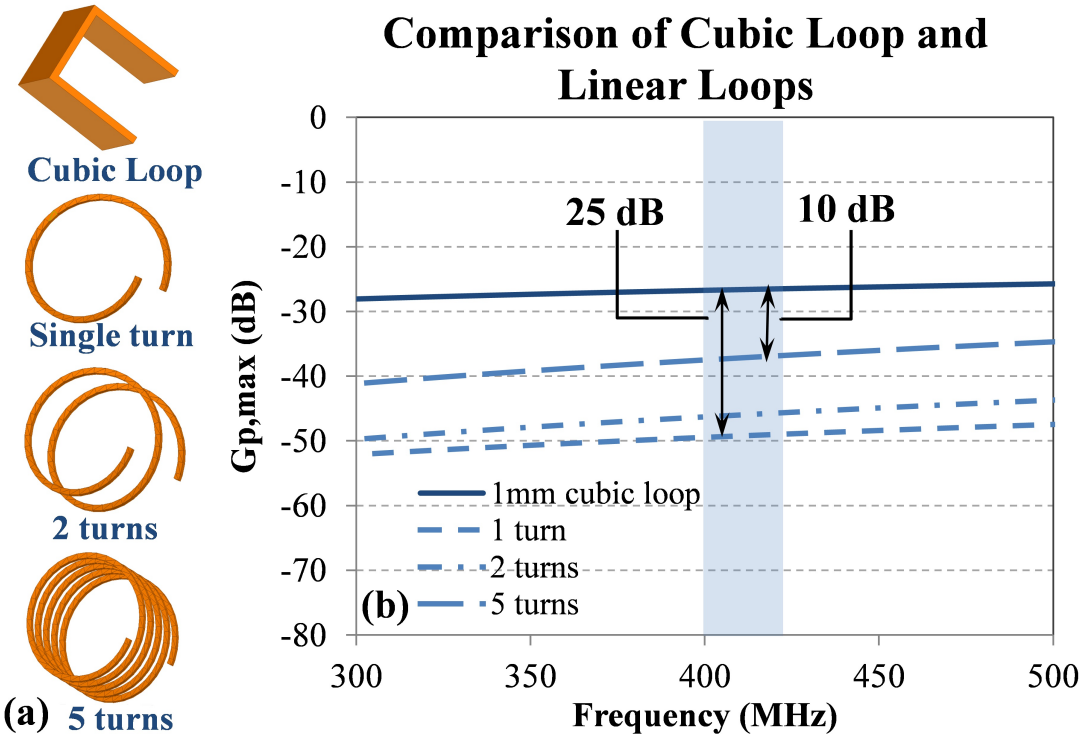

Figure 4.15: Simulation of link power efficiency using cubic loop (solid) and wire loops (dashed).

CHAPTER 5

Simulations of Brain-Machine Interface Antennas: Effects of Environment

5.1 Antennas Integrated in Implantable Medical Systems

For the wireless links between implanted antenna inside a human body and transmitting antennas in the free space, implanted antennas are commonly placed inside biological tissues with a buffer layer, to reduce the large absorption due to direct contact and to improve biocompatibility. The buffer layer is typically made of organic polymers such as PDMS [62].

5.2 Antennas in the Layered Spherical Head Model

As an approximation, the human head is represented in this section by a multi-layered lossy dielectric sphere with the electric properties of skin, fat, skull, dura, cerebrospinal fluid (CSF) and brain. Table 5.3 shows the electric characteristics (relative dielectric constant and conductivity) of the biological tissues in the model of the spherical head at 402 MHz.

We construct different layered models, homogeneous head, four-layer head, and six-layer head, from simple to complex, to represent human head by changing the parameters of the spherical head models. The homogeneous head ignore other layered tissues and only represent the brain tissue as a sphere. The four-layered head consists of brain, CSF, skull and skin, and the six-layered head consists of brain, CSF, dura, skull, fat, and skin [63]. Dimensions of layers used in different models are shown in Table 5.2.

To investigate the effects of head tissue on the link characteristics, we simulated the antenna link in different layered head models. Configuration of loop antennas follows the

Table 5.1: Electrical properties of biological tissues in the layered head model at 402 MHz.

Head Tissue	Relative Permittivity (ϵ_r)	Conductivity ($\sigma, S/m$)	Mass Density (g/cm^2)
Brain	49.7	0.59	1.04
CSF	71.0	2.25	1.01
Dura	46.7	0.83	1.01
Skull	17.8	0.16	1.88
Fat	11.6	0.08	0.92
Skin	46.7	0.69	1.01

Table 5.2: Outer Radius of layers in different layered head model.

Head Tissue	Homogeneous Head (mm)	4-Layered Head (mm)	6-Layered Head (mm)
Brain	90.0	82.0	82.0
CSF	—	84.0	86.0
Dura	—	—	86.5
Skull	—	85.5	87.6
Fat	—	—	89.0
Skin	—	90.0	90.0

design presented in Chapter 4. Again the implanted antenna is immersed into the region of CSF, as illustrated in Fig. 5.1.

5.3 Antennas in Fully-Integrated Human Head Model

The integrated ANSYS man's head model incorporates the detailed structures, e.g. the organs and muscles. The model contains the original geometries without simplification. It generates about half a million tetrahedra in full wave simulation.The materials of biological

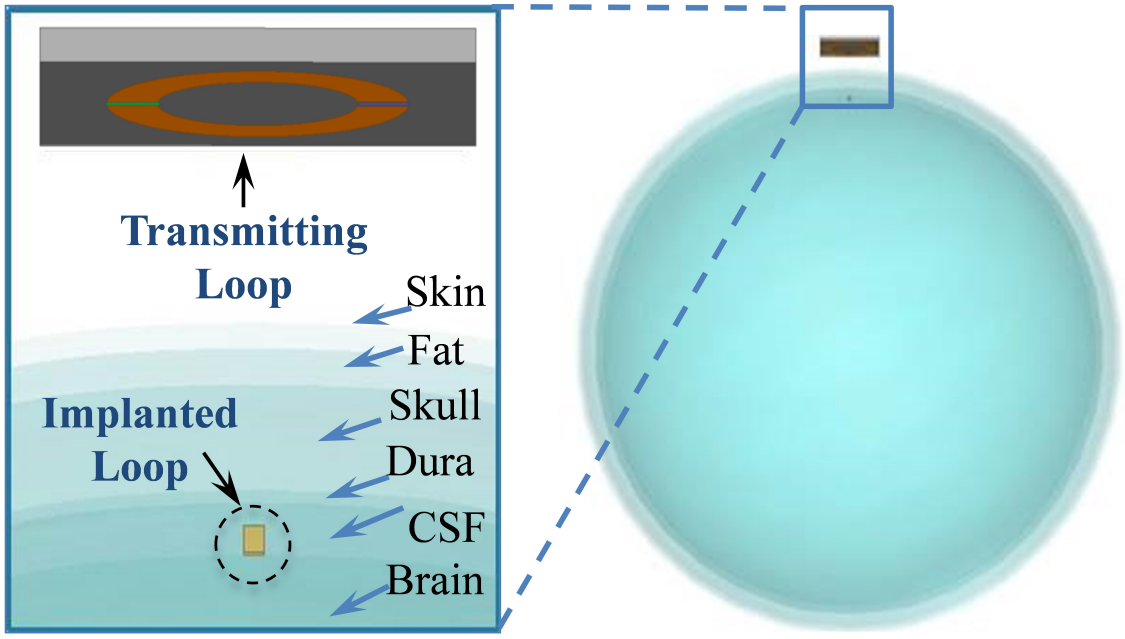

Figure 5.1: Antenna configuration in layered head model.

tissues are characterized by a frequency-dependent relative permittivity ϵ_r and a frequency-dependent conductivity σ, and is thus more accurate than the layered head through all the frequency band [64]. Again the antenna configuration remains the same as described in the previous chapter, as shown in Fig. 5.2.

5.4 Effects of Biological Tissues

5.4.1 Path Loss in Head Tissues

To investigate the effect that tissue has on the link characteristics, the same antenna setup is generated in different air and different head models and results are compared and discussed. However the frequency associated with the optimum link efficiency has not shifted noticeably.

As expected, the link loss when operating in air is lower than when operated through tissue across the entire frequency band. At lower frequencies the difference decreases, while in high frequencies it clearly increases. This can be explained by the increased E-field produced by the loop at higher frequencies, leading to higher interaction with the tissue.

Table 5.3: Electrical properties of biological tissues in the layered head model at 402 MHz.

Head Tissue	Relative Permittivity (ϵ_r)	Conductivity ($\sigma, S/m$)	Mass Density (g/cm^2)
Brain	49.7	0.59	1.04
CSF	71.0	2.25	1.01
Skull	17.8	0.16	1.88
Skin	46.7	0.69	1.01
Spinal cord	35.4	0.45	1.04
Muscle	58.8	0.84	1.04
Cartilage	45.4	0.59	1.10
Cerebellum	55.9	1.03	1.05
Eye tissue	57.7	1.00	1.17
Tongue	57.7	0.77	1.05
Blood	64.2	1.35	1.06
Teeth	22.4	0.23	1.85
Trachea	44.2	0.64	1.10

Simulation results of the link power efficiency generated in the two head models agree very well, with only a difference of 1 dB at the frequency around 400 MHz. We further observed that as the frequency goes to higher regime the effects of the detailed structures start to appear and difference between the two models increases. The presence of tissue also affects the impedances of antennas, or impedance of the two port network, in a way to increase the resistance, which also agrees with our expectation with the lossy medium.

5.4.2 Local SAR Generated in Tissues

The amount of power available in the wireless link is limited by the path loss as well as the maximum transmit power regulated to avoid adverse effects on tissues due to exposure to electromagnetic field. Based on the standard for safety level of human exposure to high

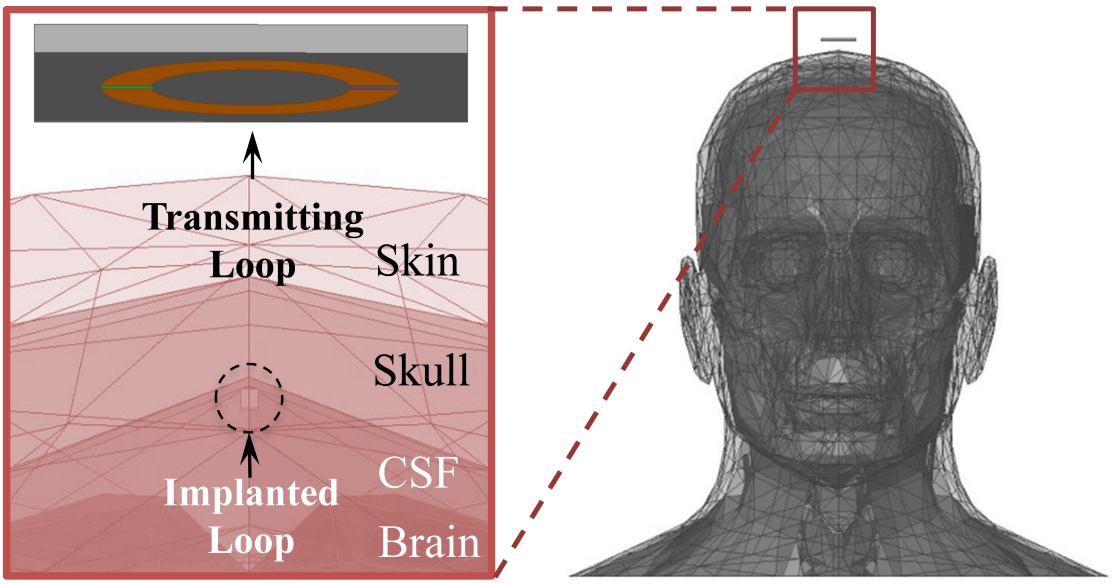

Figure 5.2: Antenna configuration in ANSYS man's head model.

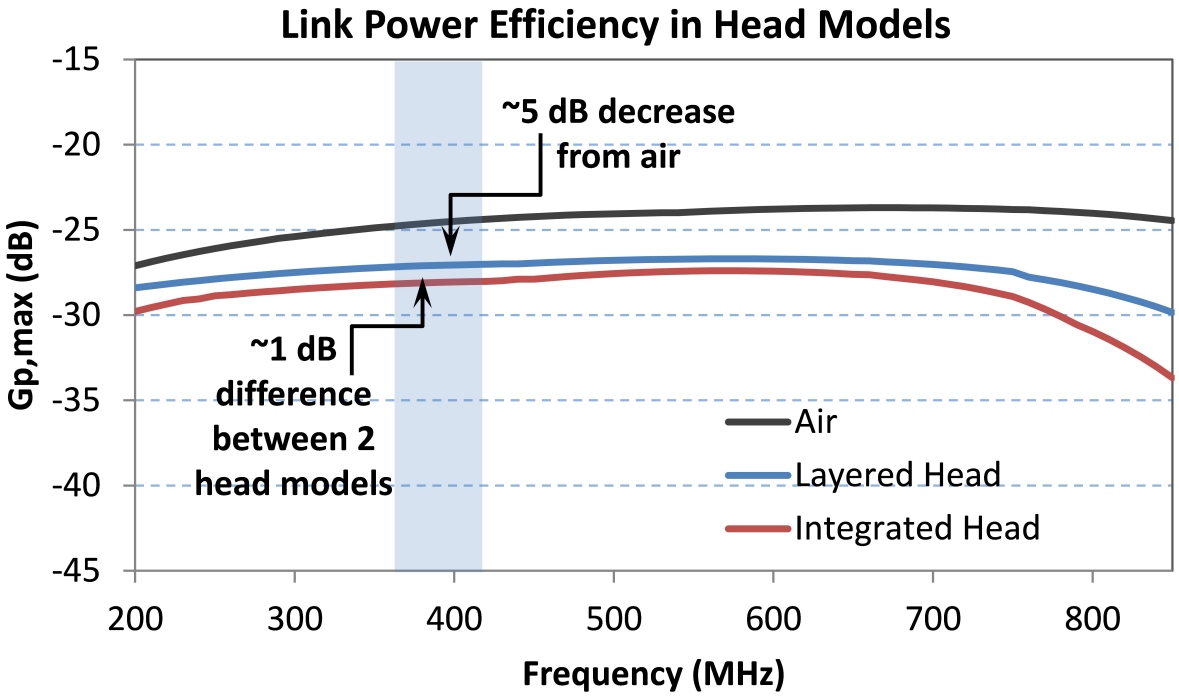

Figure 5.3: Simulated link power efficiency generated by the antenna system in the layered head model and integrated head model.

frequency electromagnetic field from 100 kHz to 300 GHz, limits in terms of the specific absorption rate (SAR) are regulated to protect human body from adverse health effects due to tissue heating [65]. The SAR is a measure of power level that absorbed by a certain amount of tissue and converted into heat. The limit is based on a certain amount of tissue heating associated with the electromagnetic radiation it is exposed to, and therefore defines the maximum transmit power of wireless devices. In the U.S. standard, the SAR value for partial body exposure regulated by FCC to 1.6 W/kg over 1 gram of tissue. Based on definition given by standards, the SAR is determined by the electric field by:

$$SAR = \frac{\sigma |E|^2}{\rho} \tag{5.1}$$

where σ represents the conductivity on tissue, ρ represents the mass density of the tissue, and E is the RMS value of the local electric field in tissue.

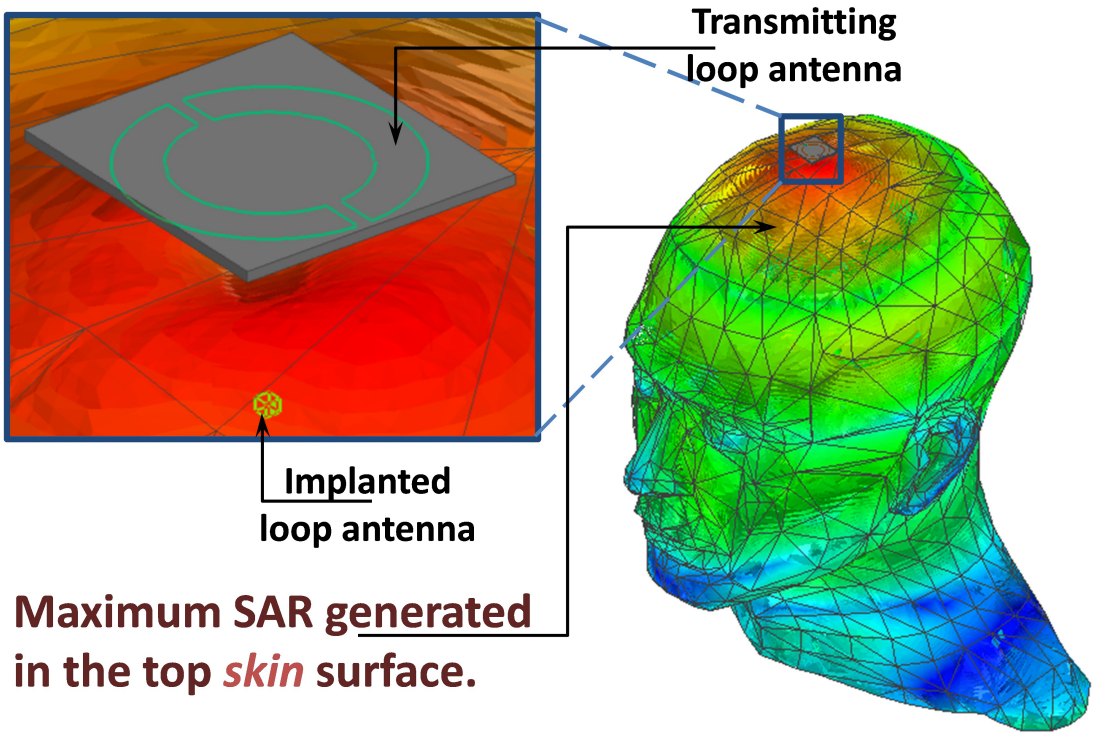

Figure 5.4: Simulated SAR generated by the antenna system in the ANSYS man's head model.

Table 5.4: Effects of the head tissue on overall power delivered to the load.

Media (At 400 MHz)	SAR_{max}, W/kg	$P_{t,max}$, dBm	$G_{p,max}$, dB	$P_{L,max}$, dBm
Homogeneous Head	21.9	18.6	-26.9	-8.3
4 Layered Head	22.4	18.5	-27.0	-8,5
6 Layered Head	22.5	18.5	-27.4	-8.9
Integrated Head	26.7	17.8	-28.1	-10.2

In order to find the maximum transmit power compliant to the SAR limitation, we compare it with the maximum SAR generated from the build-in function of HFSS in the ANSYS head model simulation with the testing excitation at the transmitting port assigned as 1 W. As shown in Fig 1, the maximum SAR is generated in the top skin surface, which is the closest tissue to the transmitting loop antenna. As we compare the simulation with the regulated limitation, the maximum SAR-compliant transmit power was calculated as 60 mW or 17.8 dBm at the frequency of 400 MHz. Since the impedance mismatch loss was already taken into account in the simulation of link power efficiency, here the simulation of maximum SAR assumed that all the antenna ports are conjugate matched.

5.4.3 Effects on Antenna Impedances

For a fixed maximum receive power, the maximum available voltage is also related to the impedance at resonance, which to the first order increases with frequency, and affected by the presence of head tissue as well.

Simulations of antenna impedances, or the impedances of the two port network shown in Table 5.5 predict the influence introduced by the presence of tissue, in a way to increase the resistance. This also agrees with our expectation that the path loss in channel can be represented by increasing of antenna resistance.

Table 5.5: Effects of the head tissue on impedance of antennas.

Media (At 400 MHz)	Implanted Antenna R_{ra}	Implanted Antenna X_{ra}	Tranmitting Antenna R_{ta}	Transmitting Antenna X_{ta}
Air	0.0344 Ω	1.81 Ω	0.21 Ω	38.8 Ω
Homogeneous Head	0.0376 Ω	1.24 Ω	0.34 Ω	38.5 Ω
4 Layered Head	0.0310 Ω	1.84 Ω	0.31 Ω	40.9 Ω
6 Layered Head	0.0408 Ω	2.14 Ω	0.32 Ω	41.2 Ω
Integrated Head	0.0461 Ω	2.17 Ω	0.39 Ω	44.5 Ω

CHAPTER 6

Fabrication and Measurement of Brain-Machine Interface Antennas

6.1 Integration of Matching Networks

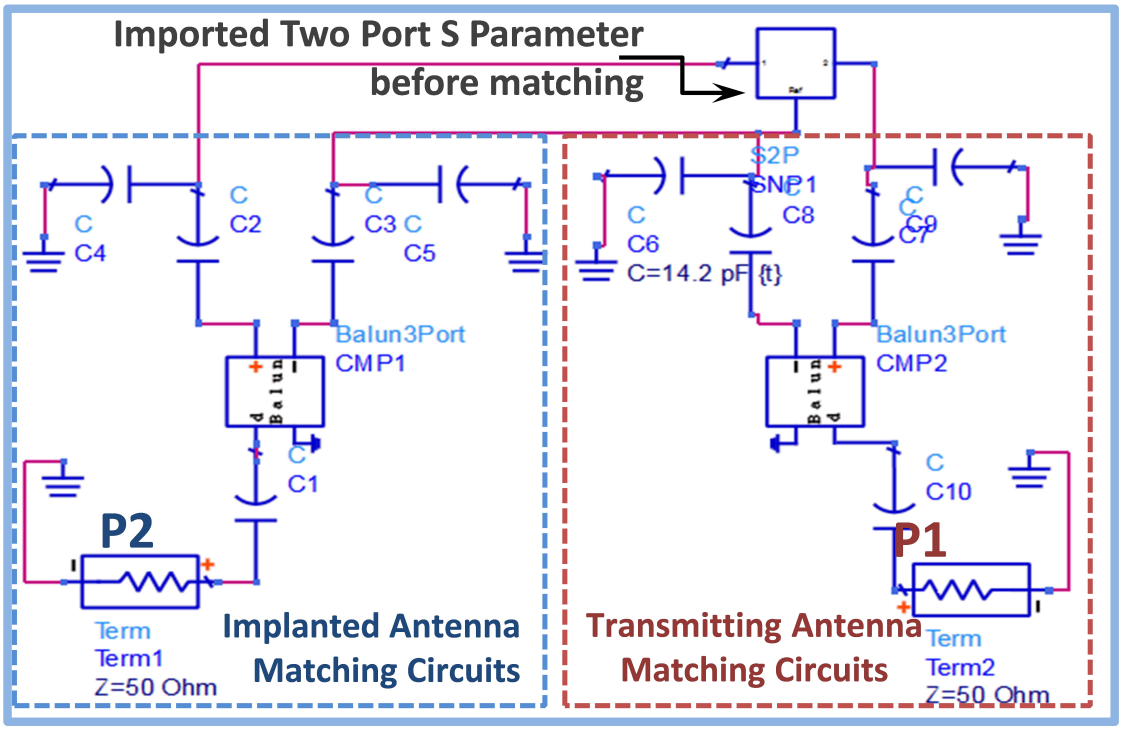

Figure 6.1: Schematics of matching circuits built in ADS.

As already mentioned previously, the impedance of the loop antennas has a small real part and large imaginary part, which would cause large reflection as it connected to a standard 50 ohm cable. To address that we integrated matching circuits with parallel and series capacitors to convert the impedance to 50 ohm, and surface-mount baluns (ATB2012-50011) [66] to

properly convert differential port to single-ended port. The matching circuits were built in ADS with the 2 port S parameters exported from HFSS, which includes simulation of wireless link between antennas and head tissue. We further simulate the link characteristics including mismatch. Now with the matching circuits we have reflection on both the 2 ports lower than -15 dB, and the overall coupling efficiency is as high as -20 dB. This combined with the maximum SAR-compliant transmit power based on the analysis in 5.4.2, satisfies the requirements for neural recoding with hundreds of channels [67].

6.2 Fabrication of Antenna Prototypes

The cubic copper loop was made of a 0.03-mm-thick copper plate and it was attached to the SMA connector via a small test board with matching circuits, which matches the input impedance of the implant antenna to 50 Ω. We made the circuits as small as possible to avoid EM coupling of the matching circuit to the transmitting antenna. The transmitting loop was fabricated by 31 mils RT/Ruroid 5880 High Frequency Laminates with dielectric constant of 2.20 and loss tangent of 0.0004 [68]. Similarly, the transmitting loop was attached to SMA connector via matching circuits to tune the impedance to 50 Ω.

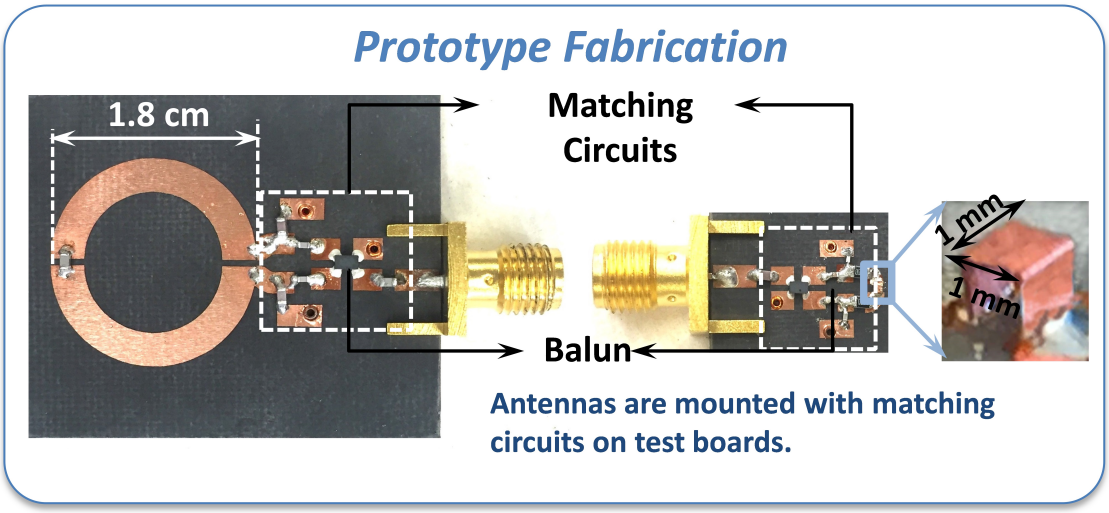

Figure 6.2: Prototypes of transmitting and implanted antennas mounted on test boards with matching circuits.

To ease the fabrication of the prototype, systematic procedures were created. The fabrication procedures starts with chemical etching of the double-sided PCB broad. On the top side is the transmitting loop antenna and microstrip lines for the matching circuits, while on the bottom side is the ground plane for matching circuits. The second step is to drill 3 holes for each of the matching circuits and install vias to ground the circuits and baluns properly. The third step is to connect the surface-mount balun to the broad with conductive epoxy. The reason to use epoxy is due to difficulty of soldering multiple small pins underneath as well as the temperature requirements. Finally all the capacitors and SMA connectors are carefully soldered to the broad. And with that, the prototype is completed.

6.3 Measurement Setup

The Two-port measurement was carried out as the antennas aligned as shown in Fig. 6.3. The two ports of VNA are connected to the transmitting and receiving antennas through SMA connectors.

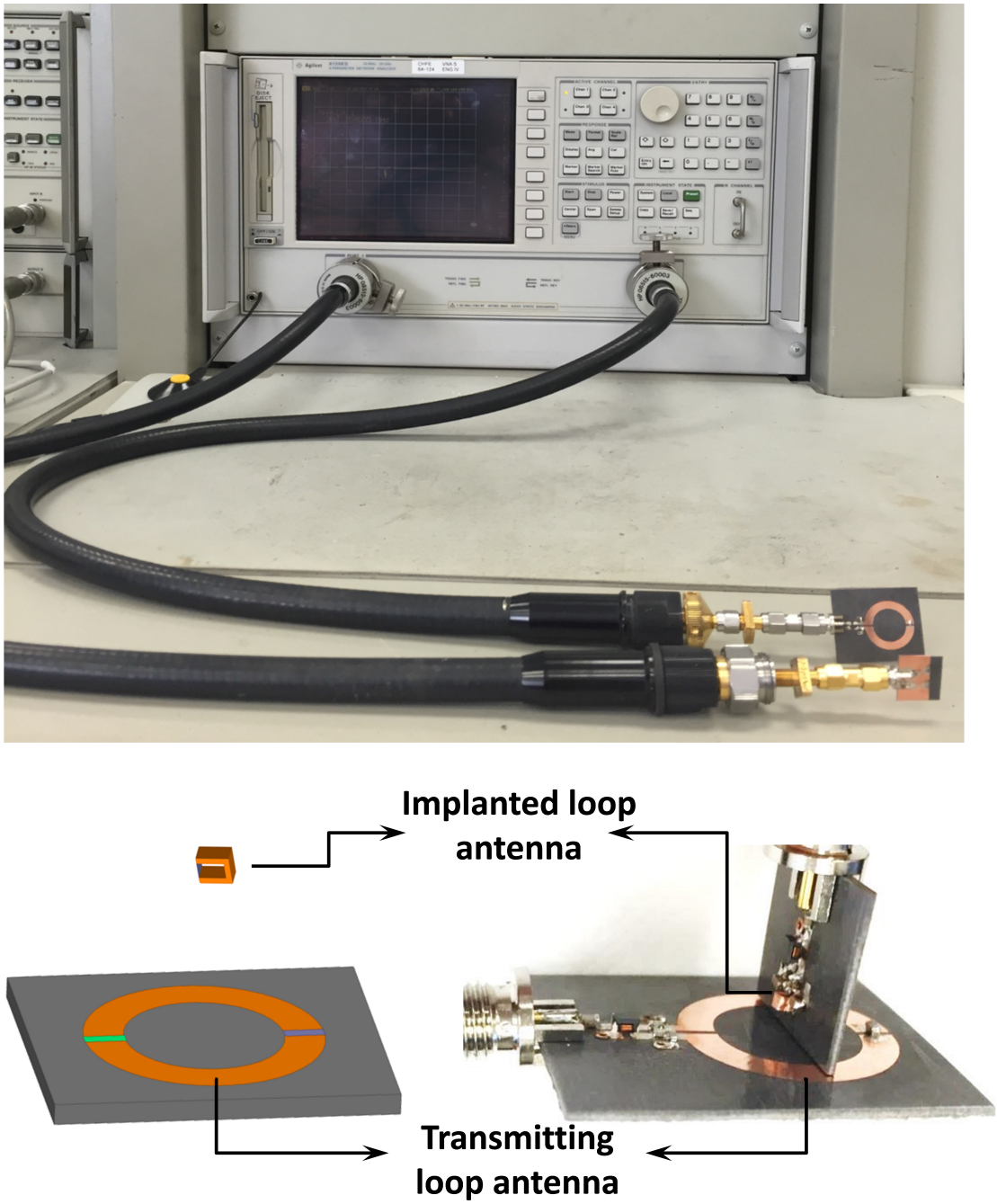

Figure 6.3: Measurement setup of the BMI antennas.

6.4 Measurement Results of Designed Antennas

After the standard VNA parameter setting and calibration, the two-port Z parameters was extracted and $G_{p,max}$ was calculated according to (4.6) and (4.7) (see the MATLAB code

in Appendix D). As shown in Fig. 6.4, the two-port measurement results demonstrate S_{11} and S_{22} below -10 dB and the maximum realized $G_{p,max}$ of -20 dB, with a -30 dB $G_{p,max}$ bandwidth of 10 MHz.

To characterize the robustness of the design, we further investigated the effects of different separations between transmitting and implanted antennas. The coupling efficiency was measured for distance between loop centers from 3 mm to 15 mm and plotted for the points where maximum coupling occurs with the changing separation. As expected, the coupling decreased with the increasing separation. As mentioned in the previous section, increasing the transmitting loop-to-skin distance decreases SAR in the tissues, but this is at the expense of lower link power efficiency.

Effects of lateral misalignment between the loop centers were also studied by measurement, as illustrated in Fig. 6.7. Again the coupling efficiency was measured as the center shift of 5 mm and 10 mm was applied. The transmitting loop antenna was placed 5 mm above the implanted antenna. As expected, the best coupling is achieved when the transmitting and the implanted antennas are perfectly aligned while any lateral misalignment decreases the link power efficiency. From the measurement results, we observed that as the loop misaligned by 5 mm from concentric, the coupling efficiency still remained -30 dB at maximum, which is a typically accepted level for existing BMI telemetry systems [69]. Thus, the link power efficiency of the system is not very much sensitive to lateral misalignment. The effect of lateral misalignment could be potentially addressed by using transmitting antenna with larger size [56]. However, by doing this the local SAR generated in tissue would increase as well, which further limits the maximum power that can be safely transmitted and delivered to the load.

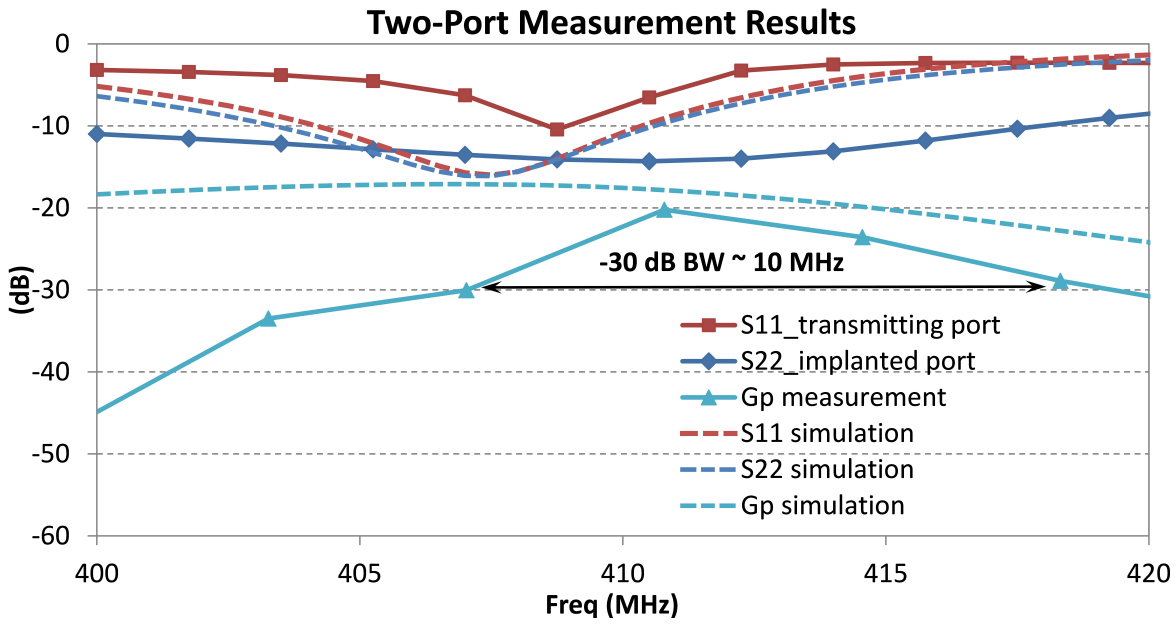

Figure 6.4: Two-port measurement for the antenna system and comparison to simulation.

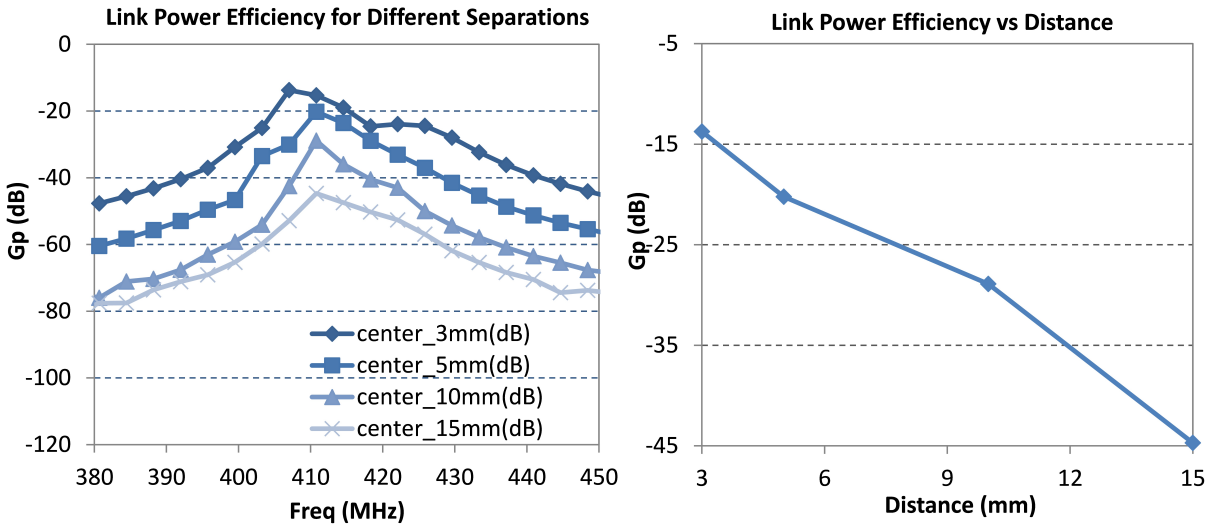

Figure 6.5: Two-port measurement for the antenna system, study of effects of separations.

6.5 Estimation of Channel Capacity

In order to support multichannel neural recoding systems, the telemetry system was designed to transfer both power and data, thus it is necessary to estimated the channel capacity of

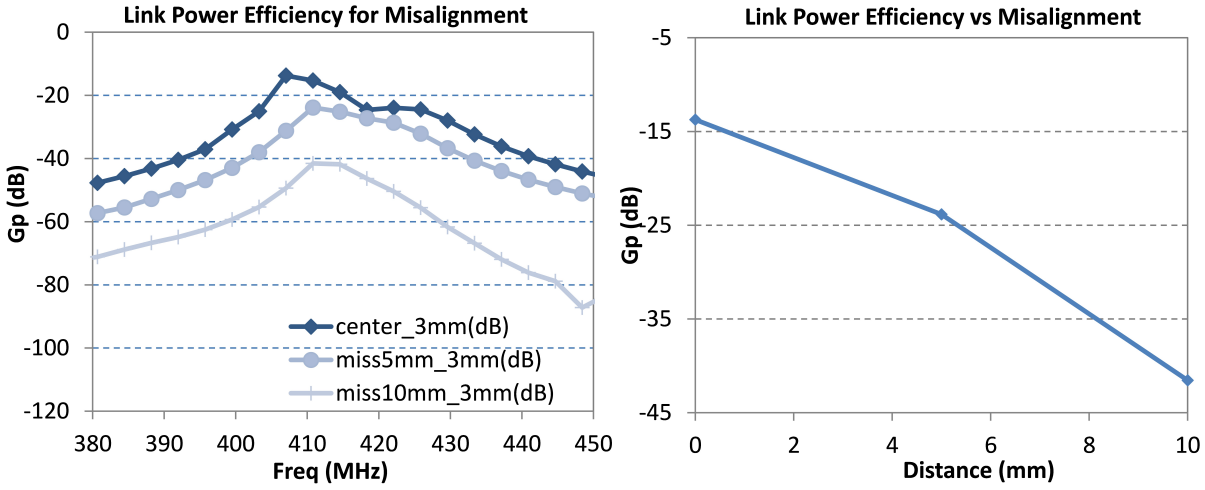

Figure 6.6: Two-port measurement for the antenna system, study of effects of lateral misalignment.

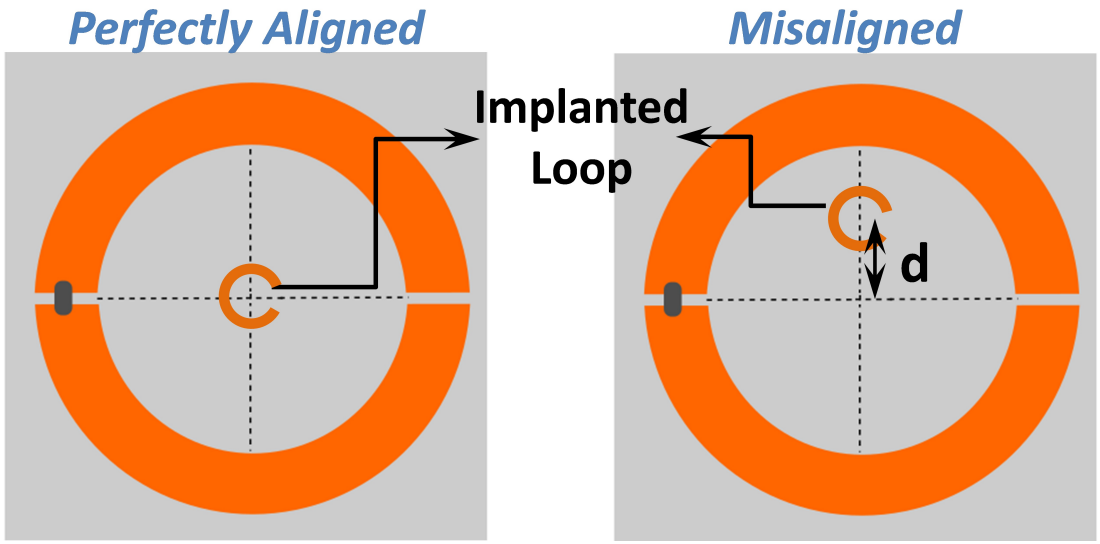

Figure 6.7: Lateral misalignment between transmitting and implanted loop from concentric.

the proposed antenna system from both power and data point of views.

For power transfer, the link budget gives the amount of energy supplied to the load, which is related to the maximum SAR compliant transmit power and the maximum link

power efficiency:

$$P_L = G_{p,max} P_{t,max} \tag{6.1}$$

where $P_{t,max}$ represents the maximum SAR-compliant transmit power and $G_{p,max}$ represents the maximum link efficiency. According to previous discussion, the maximum amount of power supplied to the load is 600 μW or -2 dBm, which is related to the maximum SAR compliant transmitting power of 60 mW or 18 dBm and the maximum link power efficiency of -20 dB. For the existing neural recording ICs, the achievable power dissipation can be as low as 5 μW/channel [67]. Thus the system can power up existing neural recording ICs with up to 120 channels.

Table 6.1: Estimation of power capacity by link budget.

$P_{t,max}$	$G_{p,max}$	P_L	Channels
60 mW (18 dBm)	-20 dB	600 μW (-2 dBm)	120 channels

For data transfer, the data capacity is related to bandwidth and signal to noise ratio by Shannons law:

$$C = BW log_2(1 + SNR) \tag{6.2}$$

where C is the data capacity in bits per second, BW is the bandwidth of the system in hertz, and SNR the signal-to-noise ratio (SNR) of the signal. with a -30 dB bandwidth of 10 MHz. For the existing neural recording ICs [70], a bandwidth of 10 MHz can support data flow of 0.3 Mbps for up to 100 recording channels with a data rate of 0.3 Mbps. The telemetry system presented here thus satisfies the requirements for future clinical BMIs with high-speed neural recordings of large populations of neurons to reconstruct complex neural activities with multiple degrees of freedom [40].

CHAPTER 7

Conclusion and Future Works

Radio frequency identification (RFID) technology in the ultra-high frequency (UHF) band has become the mainstream applications that help the speed of handling manufactured goods and materials in recent years. In an RFID system, the tag antenna plays an important role in the overall system performance. To date, most miniaturized tag antennas are linearly polarized. In the first part of the thesis, a circularly polarized cross-dipole RFID tag antenna design was presented. The CP mode was excited by two orthogonal dipoles with 90 degree phase delay between each other. Impedance matching between tag antenna and the chip was achieved using a matching structure of T-match meander line. The triangular-shaped ending was used for achieving a compact design. Such novel tag antenna structure with CP characteristics could potentially enhance the tag sensitivity by up to 3 dB compared with LP tags, which is desirable for the development of miniature and highly-sensitive RFID systems.

The mechanism of RFID backscattering technique has been utilized for many novel wireless sensing applications, such as remote health sensing, and biomedical signal recoding. In the second part of the thesis, an antenna system for wireless neural recording based on RFID inspired backscattering technique was proposed. Power and data transfer was achieved by near field inductive coupling between transmitting antenna and implanted antenna. The power received by the implanted antenna activates the neural recording IC. Similar to the operating mechanism of any passive RFID tags, the data link was established through the modulation of the impedance at the terminal of the implant antenna according to the acquired neuro signal. Such novel design of BMI antennas constitutes important milestone in the development of wireless BMI systems, and enhances wireless body-centric systems.

The antenna system for BMIs presented in this thesis is more of a first step rather then

the final step in developing miniature implanted neural recoding systems. A lot of work need to be carry on to build a complete system that is viable for clinical applications.

Integrating the antenna system with a ultra-low power neural recoding IC to evaluate the overall system performance is one crucial step for the entire concept to be realized. Building small and efficient external interrogator is also one critical area to be concerned in future work. For the external transmitting antenna the ultimate goal is to fabricate it to be clothing-integrated and wearable. This requires knowledge of the properties of different types of wearable conductive materials. The realized link power gain between antennas still has room to be improved. Integrating metamaterial shell might be a way to enhance the overall link efficiency and is therefore worthwhile to look at. As a final step, encapsulation of the implanted system in a bio-compatible package and its effect on the wireless power transfer is another issue that needs to be carefully addressed before it can be implanted in humans.

Appendix A

The Polarization Loss Factor between Antennas

Generally speaking the polarization of a receiving antenna could be different to the polarization of the incoming electromagnetic wave. The power loss due to this mechanism is commonly referred as polarization mismatch and can be represented by the polarization loss factor, as shown in (2.1). Assuming the electric field is time-harmonic with the time variation represented by $e^{j\omega t}$, the incoming wave can be written as:

$$\mathbf{E_i} = \hat{\rho}_\mathbf{w} E_i \tag{A.1}$$

where $\hat{\rho}_\mathbf{w}$ is the unit vector of the incident wave. Assuming an elliptically polarized incident wave is traveling in the inward radial direction, the unit vector is written as:

$$\hat{\rho}_\mathbf{w} = (\frac{A_w \hat{\mathbf{a}}_\theta + jB_w \hat{\mathbf{a}}_\phi}{\sqrt{A_w^2 + B_w^2}}) \tag{A.2}$$

where A_w and B_w are the magnitudes of incident wave in θ and ϕ directions, as defined in Fig A.1.

Similarly, the polarization of the electric field of the receiving antenna can be expressed as:

$$\mathbf{E_r} = \hat{\rho}_\mathbf{r} E_r \tag{A.3}$$

where $\hat{\rho}_\mathbf{r}$ is the unit polarization vector of the receiving antenna, and is written as:

$$\hat{\rho}_\mathbf{r} = (\frac{A_r \hat{\mathbf{a}}_\theta - jB_r \hat{\mathbf{a}}_\phi}{\sqrt{A_r^2 + B_r^2}}) \tag{A.4}$$

with A_r and B_r representing the magnitudes of receiving wave in θ and ϕ directions. Note that since the polarization of receiving antenna is defined in its transmitting mode, and

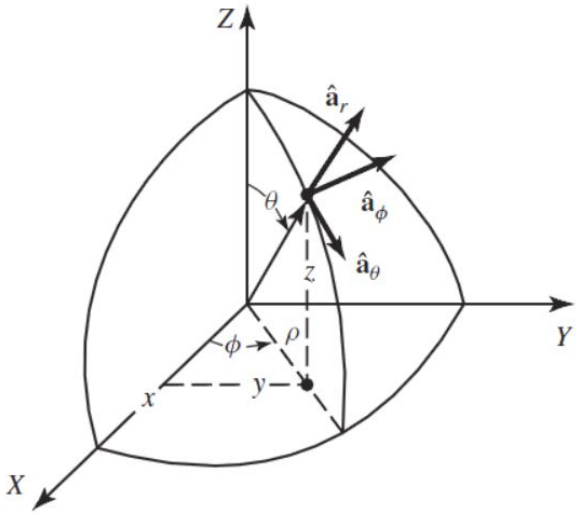

Figure A.1: Spherical coordinate system and unit vectors [71].

transmitting and receiving waves are viewed from different direction, the opposite sign appears in (A.4) and (A.2). However the receiving antenna has the same sense of polarization as it is in the transmitting mode.

The polarization mismatch can be taken into account by the polarization loss factor defined as [71]:

$$\tau_{PLF} = |\hat{\rho}_{\mathbf{w}} \hat{\rho}_{\mathbf{r}}|^2 \tag{A.5}$$

Note that since the polarization vector of the transmitting antenna is defined exactly as the polarization of incident wave it is generated, (A.5) not only refers to the polarization loss between an incoming wave and a receiving antenna, also defines the polarization mismatch between transmitting and receiving antennas that are not perfectly aligned. If the antennas are polarization matched, the τ_{PLF} will be unity and the receiving antenna will extract the maximum power from the transmitting antenna. If the antennas are aligned orthogonally, then there will be no power extracted by the receiving antenna. Two antennas that are both circularly polarized in the same sense (both RHCP or LHCP) do not suffer signal loss due to polarization mismatch, while a linearly polarized receiving antenna will have a polarization mismatch loss of 0.5 (-3 dB) with a circularly polarized transmitting antenna, no matter

what the angle the receiving antenna is rotated to.

As a special case with a CP transmitting antenna and an elliptically polarized receiving antenna, the polarization loss factor τ_{PLF} can be written as a function of AR of the receiving antenna [72]:

$$\tau_{PLF} = \frac{1}{1+e^2}, e = \frac{AR-1}{AR+1} \tag{A.6}$$

as was applied in the fitness function of CP tag antenna optimization in (3.2).

Appendix B

MATLAB Code of S_{11} Calculation for Conjugate Matching

```
% See Equation (3.1).

T1=importdata('Z11re.csv');
T1data=T1.data;
freq=T1data(1:end,1);
Z11re=T1data(1:end,3);
Z11Length=length(Z11re);
T2=importdata('Z11imag.csv');
T2data=T2.data;
Z11imag=T2data(1:end,2);
Za=transpose(Z11re+1j*Z11imag);
Zc=24-195*1j.*ones(1,Z11Length);
Zc=(14.56-161.25*1j).*ones(1,Z11Length);
S11dB_thickness=20.*log10(abs((Za-conj(Zc))./(Za+Zc)));
S11_abs=abs((Za-conj(Zc))./(Za+Zc));
vswr=(1+S11_abs)./(1-S11_abs);
plot(freq,S11dB);
makeFig.Nice;
```

Appendix C

MATLAB Code of Z_A Calculation in Differential Measurement

```
% See Equation (3.9) and (3.10).

T1=importdata('7_7.csv');
T1data=T1.data;
freq=T1data(1:end,1)-1e8;
S11magdB=T1data(1:end,2); S11phase=T1data(1:end,3);
S21magdB=T1data(1:end,4);      S21phase=T1data(1:end,5);
S12magdB=T1data(1:end,6);    S12phase=T1data(1:end,7);
S22magdB=T1data(1:end,8);    S22phase=T1data(1:end,9);
S11=10.^(S11magdB/10).*exp(1i*S11phase*pi/180);
S21=10.^(S21magdB/10).*exp(1i*S21phase*pi/180);
S12=10.^(S12magdB/10).*exp(1i*S12phase*pi/180);
S22=10.^(S11magdB/10).*exp(1i*S22phase*pi/180);
Zd = 2*50*(1-S11.*S22+S12.*S21-S21-S12)./((1-S11).*(1-S22)-S21.*S12);
Zdre=real(Zd);   Zdim=imag(Zd);
plot(freq, Zdre);
hold on
plot(freq, Zdim,'r');
```

Appendix D

MATLAB Code of $G_{p,max}$ Calculation by 2-Port Z Parameters

```
% See Equation (4.6) and (4.7).

T11=importdata('z11.csv');   T11data=T11.data;
T22=importdata('z22.csv');   T22data=T22.data;
T12=importdata('z12.csv');   T12data=T12.data;
T21=importdata('z21.csv');   T21data=T21.data;
freq=T11data(1:end,1);
Z11im=T11data(1:end,2);  Z11re=T11data(1:end,3);  Z11=Z11re+1j*Z11im;
Z22im=T22data(1:end,2);  Z22re=T22data(1:end,3);  Z22=Z22re+1j*Z22im;
Z12im=T12data(1:end,2);  Z12re=T12data(1:end,3);  Z12=Z12re+1j*Z12im;
Z21im=T21data(1:end,2);  Z21re=T21data(1:end,3);  Z21=Z21re+1j*Z21im;
S=2*real(Z11).*real(Z22)-real(Z12.*Z21);
Gpmax=(abs(Z21)).^2./(S+(S.^2-(abs(Z12.*Z21)).^2).^0.5);
Gpmax_dB=10*log10(Gpmax);
plot(freq*1000,Gpmax_dB);
xlabel('freq (MHz)');  ylabel('Gpmax (dB)');
```

References

[1] H. Stockman, "Communication by means of reflected power," *Proceedings of the IRE*, vol. 36, no. 10, pp. 1196–1204, 1948.

[2] K. Finkenzeller, *RFID Handbook: Radio-frequency identification fundamentals and applications*. Wiley, 1999.

[3] "Barcoding Inc," http://blog.barcoding.com/2008/07/rfid-readers/, 2008.

[4] "Adventech," http://www.advantech-inc.com/rfid.html, 2014.

[5] C. Cho, H. Choo, and I. Park, "Design of planar RFID tag antenna for metallic objects," *Electronics Letters*, vol. 44, no. 3, pp. 175–177, 2008.

[6] Y. Choi, U. Kim, J. Kim, and J. Choi, "Design of modified folded dipole antenna for UHF RFID tag," *Electronics letters*, vol. 45, no. 8, pp. 387–389, 2009.

[7] H.-W. Liu, C.-F. Yang, and C.-H. Ku, "Novel miniature monopole tag antenna for UHF RFID applications," *Antennas and Wireless Propagation Letters, IEEE*, vol. 9, pp. 363–366, 2010.

[8] P. H. Yang, Y. Li, L. Jiang, W. Chew, and T. T. Ye, "Compact metallic RFID tag antennas with a loop-fed method," *Antennas and Propagation, IEEE Transactions on*, vol. 59, no. 12, pp. 4454–4462, 2011.

[9] B. D. Braaten, M. Reich, and J. Glower, "A compact meander-line UHF RFID tag antenna loaded with elements found in right/left-handed coplanar waveguide structures," *Antennas and Wireless Propagation Letters, IEEE*, vol. 8, pp. 1158–1161, 2009.

[10] H.-D. Chen, C.-Y.-D. Sim, and S.-H. Kuo, "Compact broadband dual coupling-feed circularly polarized RFID microstrip tag antenna mountable on metallic surface," *Antennas and Propagation, IEEE Transactions on*, vol. 60, no. 12, pp. 5571–5577, 2012.

[11] H.-D. Chen, C.-H. Tsai, C.-Y.-D. Sim, and C.-Y. Kuo, "Circularly polarized loop tag antenna for long reading range RFID applications," *Antennas and Wireless Propagation Letters, IEEE*, vol. 12, pp. 1460–1463, 2013.

[12] C. Cho, I. Park, and H. Choo, "Design of a circularly polarized tag antenna for increased reading range," *Antennas and Propagation, IEEE Transactions on*, vol. 57, no. 10, pp. 3418–3422, 2009.

[13] J.-H. Lu and B.-S. Chang, "Planar circularly polarized tag antenna with compact operation for UHF RFID application," *Journal of Electromagnetic Waves and Applications*, vol. 27, no. 15, pp. 1882–1891, 2013.

[14] J. Grosinger, *Backscatter radio frequency systems and devices for novel wireless sensing applications*. PhD Dissertation, 2012.

[15] A. Rida, L. Yang, and M. Tentzeris, *RFID-enabled sensor design and applications*. Artech House, 2010.

[16] G. Marrocco, "Rfid antennas for the uhf remote monitoring of human subjects," *Antennas and Propagation, IEEE Transactions on*, vol. 55, no. 6, pp. 1862–1870, 2007.

[17] "How Can RFID Technology Benefit Healthcare Facilities?"

[18] R. P. Rao, *Brain-computer interfacing: an introduction*. Cambridge University Press, 2013.

[19] M. A. Nicolelis, "Actions from thoughts," *Nature*, vol. 409, no. 6818, pp. 403–407, 2001.

[20] S. Rao, N. Llombart, E. Moradi, K. Koski, T. Bjorninen, L. Sydanheimo, J. M. Rabaey, J. M. Carmena, Y. Rahmat-Samii, and L. Ukkonen, "Miniature implantable and wearable on-body antennas: towards the new era of wireless body-centric systems [antenna applications corner]," *Antennas and Propagation Magazine, IEEE*, vol. 56, no. 1, pp. 271–291, 2014.

[21] J. M. Rabaey, "Brain-machine interfaces as the new frontier in extreme miniaturization," in *Solid-State Device Research Conference (ESSDERC), 2011 Proceedings of the European*. IEEE, 2011, pp. 19–24.

[22] H. H. Tran, S. X. Ta, and I. Park, "A compact circularly polarized crossed-dipole antenna for an RFID tag," *Antennas and Wireless Propagation Letters, IEEE*, vol. 14, pp. 674–677, 2015.

[23] G. Zamora, S. Zuffanelli, F. Paredes, F. Martin, and J. Bonache, "Design and synthesis methodology for UHF RFID tags based on the t-match network," *Microwave Theory and Techniques, IEEE Transactions on*, vol. 61, no. 12, pp. 4090–4098, 2013.

[24] S. X. Ta, J. J. Han, and I. Park, "Compact circularly polarized composite cavity-backed crossed dipole for GPS applications," *Journal of electromagnetic engineering and science*, vol. 13, no. 1, pp. 44–49, 2013.

[25] S. X. Ta, H. Choo, I. Park, and R. W. Ziolkowski, "Multi-band, wide-beam, circularly polarized, crossed, asymmetrically barbed dipole antennas for GPS applications," *Antennas and Propagation, IEEE Transactions on*, vol. 61, no. 11, pp. 5771–5775, 2013.

[26] S. P. Team, "Planning for medical implant communications systems (MICS) & related devices proposals paper."

[27] M. Zargham and P. G. Gulak, "Maximum achievable efficiency in near-field coupled power-transfer systems," *Biomedical Circuits and Systems, IEEE Transactions on*, vol. 6, no. 3, pp. 228–245, 2012.

[28] E. Moradi, T. Bjorninen, L. Sydanheimo, L. Ukkonen, and J. M. Rabaey, "Analysis of wireless powering of mm-size neural recording tags in rfid-inspired wireless brain-machine interface systems," in *RFID (RFID), 2013 IEEE International Conference on*. IEEE, 2013, pp. 8–15.

[29] N. C. Karmakar, *Handbook of smart antennas for RFID systems.* Wiley Online Library, 2010.

[30] J. Weinberg, "RFID, privacy, and regulation," *RFID: Applications, Security, and Privacy*, pp. 99–136, 2006.

[31] K. S. Rao, P. V. Nikitin, and S. F. Lam, "Antenna design for UHF RFID tags: a review and a practical application," *Antennas and Propagation, IEEE Transactions on*, vol. 53, no. 12, pp. 3870–3876, 2005.

[32] G. Marrocco, "The art of UHF RFID antenna design: impedance-matching and size-reduction techniques," *Antennas and Propagation Magazine, IEEE*, vol. 50, no. 1, pp. 66–79, 2008.

[33] *Monza5 RFID tag chip datasheet*, Impinj, 3 2014, rev 1.51.

[34] *UCODE G2XM product datasheet*, NXP Semiconductors, 3 2011, rev 3.6.

[35] *Mercury 4/5 user guide*, ThingMagic, 2 2007, rev 2.4.5.

[36] J. Robinson and Y. Rahmat-Samii, "Particle swarm optimization in electromagnetics," *Antennas and Propagation, IEEE Transactions on*, vol. 52, no. 2, pp. 397–407, 2004.

[37] P. V. Nikitin, K. S. Rao, S. F. Lam, V. Pillai, R. Martinez, and H. Heinrich, "Power reflection coefficient analysis for complex impedances in rfid tag design," *IEEE Transactions on Microwave Theory and Techniques*, vol. 53, no. 9, pp. 2721–2725, 2005.

[38] X. Qing, C. K. Goh, and Z. N. Chen, "Impedance characterization of rfid tag antennas and application in tag co-design," *Microwave Theory and Techniques, IEEE Transactions on*, vol. 57, no. 5, pp. 1268–1274, 2009.

[39] D. M. Pozar, *Microwave engineering.* John Wiley & Sons, 2009.

[40] M. A. Lebedev and M. A. Nicolelis, "Brain–machine interfaces: past, present and future," *TRENDS in Neurosciences*, vol. 29, no. 9, pp. 536–546, 2006.

[41] J. K. Chapin, K. A. Moxon, R. S. Markowitz, and M. A. Nicolelis, "Real-time control of a robot arm using simultaneously recorded neurons in the motor cortex," *Nature neuroscience*, vol. 2, no. 7, pp. 664–670, 1999.

[42] J. M. Carmena, "Advances in neuroprosthetic learning and control," 2013.

[43] J. R. Wolpaw, "Brain-computer interfaces: Signals, methods, and goals," in *Neural Engineering, 2003. Conference Proceedings. First International IEEE EMBS Conference on.* IEEE, 2003, pp. 584–585.

[44] J. Turner, W. Shain, D. Szarowski, M. Andersen, S. Martins, M. Isaacson, and H. Craighead, "Cerebral astrocyte response to micromachined silicon implants," *Experimental neurology*, vol. 156, no. 1, pp. 33–49, 1999.

[45] V. S. Polikov, P. A. Tresco, and W. M. Reichert, "Response of brain tissue to chronically implanted neural electrodes," *Journal of neuroscience methods*, vol. 148, no. 1, pp. 1–18, 2005.

[46] "Gallery: Wacky-Looking Brain Cap Turns Your Thoughts Into Motion?" http://www.ecouterre.com/wacky-looking-brain-cap-turns-your-thoughts-into-motion/eeg-brain-cap-university-of-maryland-1, 2015.

[47] "Brain Computer Interface," http://www.lce.hut.fi/research/css/bci/, 2006.

[48] "Virtual World Sharpens Mind-Control," https://www.newscientist.com/article/dn12136-virtual-world-sharpens-mind-control/, 2007.

[49] "In Breadthrough Study, Paralyzed Patients Move A Robot Arm with Their Own Thoughts," http://www.popsci.com/technology/article/2012-05/video-breakthrough-study-paralyzed-patients-move-robotic-arm-their-own-thoughts, 2012.

[50] J. E. ODoherty, M. A. Lebedev, P. J. Ifft, K. Z. Zhuang, S. Shokur, H. Bleuler, and M. A. Nicolelis, "Active tactile exploration using a brain-machine-brain interface," *Nature*, vol. 479, no. 7372, pp. 228–231, 2011.

[51] K. Y. Yazdandoost and R. Kohno, "Wireless communications for body implanted medical device," in *Microwave Conference, Asia-Pacific*. IEEE, 2007, pp. 1–4.

[52] R. R. Harrison, "Designing efficient inductive power links for implantable devices," in *Circuits and Systems, 2007. ISCAS 2007. IEEE International Symposium on*. IEEE, 2007, pp. 2080–2083.

[53] A. Drossos, V. Santomaa, and N. Kuster, "The dependence of electromagnetic energy absorption upon human head tissue composition in the frequency range of 300-3000 mhz," *Microwave Theory and Techniques, IEEE Transactions on*, vol. 48, no. 11, pp. 1988–1995, 2000.

[54] U. Azad, H. C. Jing, and Y. E. Wang, "Link budget and capacity performance of inductively coupled resonant loops," *Antennas and Propagation, IEEE Transactions on*, vol. 60, no. 5, pp. 2453–2461, 2012.

[55] T. Bjorninen, L. Sydanheimo, L. Ukkonen, R. Muller, P. Ledochowitsch, and J. Rabaey, "Antenna design for wireless electrocorticography," in *Proceedings of the 2012 IEEE International Symposium on Antennas and Propagation*, 2012.

[56] J. M. Rabaey, M. Mark, D. Chen, C. Sutardja, C. Tang, S. Gowda, M. Wagner, and D. Werthimer, "Powering and communicating with mm-size implants," in *Design, Automation & Test in Europe Conference & Exhibition (DATE), 2011*. IEEE, 2011, pp. 1–6.

[57] A. S. Poon, S. O'Driscoll, and T. H. Meng, "Optimal operating frequency in wireless power transmission for implantable devices," in *Engineering in Medicine and Biology Society, 2007. EMBS 2007. 29th Annual International Conference of the IEEE*. IEEE, 2007, pp. 5673–5678.

[58] F. Fuschini, C. Piersanti, L. Sydanheimo, L. Ukkonen, and G. Falcias, "Electromagnetic analyses of near field uhf rfid systems," *Antennas and Propagation, IEEE Transactions on*, vol. 58, no. 5, pp. 1759–1770, 2010.

[59] E. Moradi, S. Amendola, T. Bjorninen, L. Sydanheimo, J. M. Carmena, J. M. Rabaey, and L. Ukkonen, "Backscattering neural tags for wireless brain-machine interface systems," *Antennas and Propagation, IEEE Transactions on*, vol. 63, no. 2, pp. 719–726, 2015.

[60] M. Mark, T. Björninen, L. Ukkonen, L. Sydänheimo, and J. M. Rabaey, "Sar reduction and link optimization for mm-size remotely powered wireless implants using segmented loop antennas," in *Biomedical Wireless Technologies, Networks, and Sensing Systems (BioWireleSS), 2011 IEEE Topical Conference on*. IEEE, 2011, pp. 7–10.

[61] "Biomedicine: The Thought Experiment," https://www.technologyreview.com/s/528141/the-thought-experiment/, 2014.

[62] Y. Rahmat-Samii and J. Kim, "Implanted antennas in medical wireless communications," *Synthesis Lectures on Antennas*, vol. 1, no. 1, pp. 1–82, 2005.

[63] Y. Rahmat-Samii, K. Kim, M. Jensen, K. Fujimoto, and O. Edvardsson, "Antennas and humans in personal communications," *Mobile Antenna Systems Handbook*, pp. 361–460, 2001.

[64] *Ansoft Human Body Model user guide*, Ansoft, 9 2008.

[65] IEEE, "C95.1-2005 IEEE standard for safety levels with respect to human exposure to radio frequency electromagnetic fields, 3 kHz to 300 GHz," 2006.

[66] *Balun transformers ATB series*, TDK, 7 2013, rev 1.01.

[67] R. Muller, S. Gambini, and J. M. Rabaey, "A 0.013 mm^2, 5 uW , DC-coupled neural signal acquisition IC with 0.5 V supply," *Solid-State Circuits, IEEE Journal of*, vol. 47, no. 1, pp. 232–243, 2012.

[68] *RT/duroid 5870 /5880 High Frequency Laminates*, Rogers Corporation, 9 2011, rev 4.15.

[69] C. W. Lee, A. Kiourti, J. Chae, and J. L. Volakis, "A high-sensitivity fully passive neurosensing system for wireless brain signal monitoring," *Microwave Theory and Techniques, IEEE Transactions on*, vol. 63, no. 6, pp. 2060–2068, 2015.

[70] R. R. Harrison, R. J. Kier, C. A. Chestek, V. Gilja, P. Nuyujukian, S. Ryu, B. Greger, F. Solzbacher, and K. V. Shenoy, "Wireless neural recording with single low-power integrated circuit," *Neural Systems and Rehabilitation Engineering, IEEE Transactions on*, vol. 17, no. 4, pp. 322–329, 2009.

[71] C. A. Balanis, *Antenna theory: analysis and design*. John Wiley & Sons, 2016.

[72] B. Y. Toh, R. Cahill, and V. F. Fusco, "Understanding and measuring circular polarization," *Education, IEEE Transactions on*, vol. 46, no. 3, pp. 313–318, 2003.